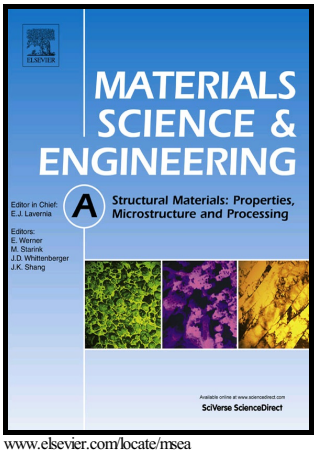
Author's Accepted Manuscript

EBSD investigation of microstructure evolution during cryogenic rolling of type 321 metastable austenitic steel

Ainur Aletdinov, Sergey Mironov, Galia Korznikova, Tatyana Konkova, Rida Zaripova, Mikhail Myshlyaev, S. Lee Semiatin



www.elsevier.com/locate/msea

PII: S0921-5093(18)31812-4
DOI: https://doi.org/10.1016/j.msea.2018.12.115
Reference: MSA37387

To appear in: *Materials Science & Engineering A*

Received date: 24 September 2018
Revised date: 25 December 2018
Accepted date: 26 December 2018

Cite this article as: Ainur Aletdinov, Sergey Mironov, Galia Korznikova, Tatyana Konkova, Rida Zaripova, Mikhail Myshlyaev and S. Lee Semiatin, EBSD investigation of microstructure evolution during cryogenic rolling of type 321 metastable austenitic steel, *Materials Science & Engineering A*, https://doi.org/10.1016/j.msea.2018.12.115

This is a PDF file of an unedited manuscript that has been accepted for publication. As a service to our customers we are providing this early version of the manuscript. The manuscript will undergo copyediting, typesetting, and review of the resulting galley proof before it is published in its final citable form. Please note that during the production process errors may be discovered which could affect the content, and all legal disclaimers that apply to the journal pertain.

ACCEPTED MANUSCRIPT

EBSD investigation of microstructure evolution during cryogenic rolling of type 321 metastable austenitic steel

Ainur Aletdinov[1], Sergey Mironov[2*], Galia Korznikova[1], Tatyana Konkova[1,3], Rida Zaripova[4], Mikhail Myshlyaev[5,6], and S. Lee Semiatin[7]

[1] Institute for Metals Superplasticity Problems, Russian Academy of Science, 39 Khalturin Str., Ufa, 450001, Russia

[2] Belgorod National Research University, Pobeda 85, Belgorod 308015, Russia

[3] University of Strathclyde, 75 Montrose Street, Glasgow, G1 1XJ, United Kingdom

[4] Ufa State Aviation Technical University, 12 K. Marx St., Ufa 450000, Russia

[5] Baikov Institute of Metallurgy and Material Science, Russian Academy of Science, 49 Lenin-av., Moscow 119991, Russia

[6] Institute of Solid State Physics, Russian Academy of Sciences, 2 Academic Osypian Str., Chernogolovka, Moscow Oblast 142432, Russia

[7] Air Force Research Laboratory, Materials and Manufacturing Directorate, AFRL/RXCM, Wright-Patterson AFB, OH 45433-7817, USA

Electron backscatter diffraction (EBSD) was employed to establish microstructure evolution in type 321 metastable austenitic stainless steel during rolling at a near-liquid-nitrogen temperature. A particular emphasis was given to evaluation of microstructure-strength relationship.

As expected, cryogenic rolling promoted strain-induced martensite transformation. The transformation was dominated by the $\gamma \rightarrow \alpha'$ sequence but clear evidence of the $\gamma \rightarrow \varepsilon \rightarrow \alpha'$ transformation path was also found. The martensitic reactions were found to occur almost exclusively within deformation bands, i.e., the most-highly strained areas in the austenite. This prevented a progressive development of deformation-induced boundaries and thus suppressed the normal grain-subdivision process in this phase. On the other hand, the preferential nucleation of martensite within the deformation bands implied a close relationship between the transformation process and slip activity in parent austenite grains. Indeed, the martensite reactions were found to occur preferentially in austenite grains with crystallographic orientations close to Goss {110}<100> and Brass {110}<112>. Moreover, the martensitic transformations were governed by preferential variant selection which was most noticeable in ε-martensite. The sensitivity of the martensitic reactions to the crystallographic orientation of the austenite grains resulted in re-activation of the transformation process after development of a deformation-induced texture in the austenitic phase at high strains. Both martensitic phases were concluded to experience plastic strain which resulted in measurable changes in misorientation distributions. Cryogenic rolling imparted dramatic strengthening resulting in a more-than-sixfold increase in yield strength. The main source of hardening was the martensitic transformation with lesser contributions from dislocations and subboundary strengthening of the austenite.

Keywords: Electron microscopy; Iron alloys; Nanocrystalline materials; Plasticity methods; Grains and interfaces; Phase transformation

[*]Corresponding author; email address: mironov@bsu.edu.ru

Accepted manuscript

ACCEPTED MANUSCRIPT

1. Introduction

The opportunity to obtain significant improvements in the mechanical properties of structural materials has prompted considerable interest in ultrafine-grain microstructures. Typically, such structures are produced by severe plastic deformation, but these techniques are relatively laborious and difficult to scale up for commercial applications. For metastable austenitic steels, however, substantial grain refinement can be achieved by conventional cold rolling followed by appropriate heat treatment. This effect is based on the phenomenon of strain-induced martensitic transformation during cold working and subsequent martensite-to-austenite reversion during annealing [1, 2]. In view of the potential advantages of this approach, it has attracted considerable interest, and a large volume of literature on the subject has been published recently [3-15]. An examination of these publications suggests however that the main emphasis in prior work has been the martensite-to-austenite reversion step. On the other hand, surprisingly little attention has been given to the strain-induced martensitic transformation despite the fact that the resulting microstructural changes heavily impact the final ultrafine-grain structure.

Microstructure evolution during the cold deformation of metastable austenitic stainless steels may be summarized briefly as follows: Due to the relatively-low stacking fault energy (SFE) of such materials, plastic straining typically leads to the dissociation of perfect dislocations into Shockley partials and stacking faults [16]. In turn, this results in planar slip and deformation banding [17]. With increasing dislocation density, the stacking faults may overlap, and, depending on the specific character of the process, this may lead to either twinning [18] or the formation of hexagonal-close-packed ε-martensite [19]. Once formed, the ε-martensite may undergo straining [3] which may lead to its transformation to body-centered-tetragonal α'-martensite [20-26]. On the other hand, the direct transformation of austenite to α'-martensite is also thought to be possible [19-22, 24-30]. In this case, the α'-martensite may nucleate at dislocation pileups [20, 19, 22, 27], mechanical twins [20, 25-30], or deformation bands [20-22, 24-25, 30]. It is well accepted that α'-martensite originates from a complex interplay between dislocations, stacking faults, and/or ε-martensite, but the mechanism is not completely clear. It is sometimes believed that the activation of a particular transformation sequence, i.e., $\gamma \rightarrow \varepsilon \rightarrow \alpha'$ versus $\gamma \rightarrow \alpha'$, is governed by the SFE. Specifically, lower SFE favors the formation of the ε-phase, whereas higher SFE promotes mechanical twinning [25]. The austenite and martensitic phases are typically found to be related through the orientation relationship $\{111\}_\gamma \parallel \{0001\}_\varepsilon \parallel \{110\}_{\alpha'}$ and $<110>_\gamma \parallel <11\text{-}20>_\varepsilon \parallel <111>_{\alpha'}$ [1, 4], although substantial deviations are sometimes reported [29]. The characteristic size of the strain-induced martensite particles as well as mechanical twins and deformation bands is usually found to be in the nanoscale range [23-36]. Therefore, even relatively-low strains imparted during conventional rolling are sufficient for the formation of ultrafine-grain structures in metastable austenitic steels [26, 29, 32-34, 36-37].

It is often suggested that lowering the rolling temperature to the cryogenic range may further enhance grain-refinement. Specifically, a reduction in temperature tends to lower the SFE and thereby promote mechanical twinning as well as ε-martensite transformation [24, 26, 34].

ACCEPTED MANUSCRIPT

Moreover, the slip/twinning threshold stress ratio also tends to decrease with temperature, thus contributing to twinning activity [36]. Last, a reduction in the deformation temperature should increase the driving force for the α'-martensitic transformation. In view of these benefits, cryogenic rolling of metastable austenitic steels has recently attracted considerable interest [26, 32-33, 36-38].

Current understanding of strain-induced martensitic transformations is still primarily based on microstructural observations from transmission electron microscopy (TEM). Despite the excellent spatial resolution of TEM, the *statistical* significance of such results may be questioned. In this regard, further insight into the pertinent phenomena may be provided by electron backscatter diffraction (EBSD) techniques which enable the quantification of microstructural details over a much larger scale. This can enable the systematic examination of microstructure changes not only in austenite but also in both of the martensitic phases, thereby providing insight into the complex interplay between these processes. However, due to the heavily-deformed character of the resulting microstructures, such observations are relatively difficult and thus still limited in number. To meet this need, high-resolution EBSD was implemented in the present work to quantify microstructure evolution during cryogenic rolling of typical metastable austenitic steel. Particular emphasis was also given to the evaluation of the broad dependence on resulting strength and microstructure.

2. Material and Experimental Procedures

The program material comprised type 321 metastable austenitic stainless steel with nominal[†] chemical composition shown in Table 1. Preliminary experiments indicated that quenching of this material into liquid nitrogen produced no martensite, and therefore it was suitable for the investigation of *strain-induced* martensitic transformations under cryogenic conditions.

The material was received as a cold-swaged bar with a cross-sectional area of 22×22 mm^2. Prior to cryogenic deformation, it was subjected to rolling to an 85-pct. thickness reduction at 950°C followed by annealing at 1200°C for 1 hour. This resulted in a fully-recrystallized austenitic grain structure with a mean grain size of ~100 μm, a high fraction of annealing twins, and a weak {111}<uvw> γ-fiber texture (supplementary Fig. S1). Microstructure observations (via backscatter electron imaging) revealed no evidence of large-scale chemical heterogeneity. Therefore, the pre-processing employed in the present work likely eliminated any possible segregation of nickel and chromium. This process produced what is referred to as the base material for the research described herein.

The base material was cryogenically rolled to various reductions in thickness, i.e., 5 pct. (true strain ≈ -0.05), 10 pct. (true strain ≈ -0.11), 15 pct. (true strain ≈ -0.16), 23 pct. (true strain ≈ -0.26), and 30 pct. (true strain ≈ -0.36). In all cases, the reduction was performed in a *single* pass using a rolling speed of 160 mm/s in a cluster mill with 65-mm-diameter work rolls. Higher

[†] According to Russian industrial standard

Accepted manuscript

ACCEPTED MANUSCRIPT

reductions were found to lead to significant (undesirable) deformation heating and roll-separating forces which exceeded the capacity of the laboratory equipment. To provide cryogenic deformation conditions, the rolling preform was soaked in liquid nitrogen and held for 15 minutes prior to rolling. The total time of the rolling process (i.e., the exposure time of the workpieces under ambient conditions) was only a few seconds. After rolling, each specimen retained a frosty appearance, thus providing evidence that deformation had indeed occurred at cryogenic temperatures. The typical flat-rolling convention was adopted in this work, i.e., the rolling, long-transverse, and thickness/normal directions were denoted as RD, TD, and ND, respectively.

To prevent static recovery and thus preserve the deformation-induced microstructures, cryogenically-rolled samples were stored in a freezer at ~-20^{o}C prior to examination. Microstructural characterization and texture analysis was performed on the mid-thickness rolling plane (i.e., the RD-TD plane) using EBSD. For this purpose, samples were prepared using conventional metallographic techniques followed by electro-polishing in a 95-pct. acetic acid + 5 pct. perchloric acid solution at near-zero-temperature (in an ice bath) with an applied potential of 30V[‡]. For EBSD, JSM-7800F and Hitachi S-4300SE field-emission-gun microscopes, both equipped with a TSL OIM^{TM} EBSD system and operating at an accelerated voltage of 25 kV, were employed.

To determine the microstructures at different length scales, several EBSD maps were acquired for each level of reduction (supplementary Table S1). Specifically, low-magnification ("overview") EBSD maps were obtained using scan step sizes ranging from 5 to 1 μm, whereas higher resolution maps were acquired with scan step sizes of 0.2, 0.1, or 0.05 μm. For each diffraction pattern, nine Kikuchi bands were used for indexing to minimize errors. The α'-martensite was indexed as a body-centered-cubic phase; this approach is believed to be feasible for EBSD of steels [39]. To ensure the reliability of the EBSD data, all grains comprising two or fewer pixels were automatically removed from the maps using the grain-dilation option of the OIM^{TM} software. Furthermore, a lower-limit boundary-misorientation cut-off of 2° was used to eliminate spurious boundaries caused by orientation noise. A 15° criterion was applied to differentiate low-angle boundaries (LABs) from high-angle boundaries (HABs).

To provide a thorough analysis of microstructural changes occurring during rolling, various microstructural characteristics were systematically examined; these included morphology, crystallographic texture, misorientation distribution as well as orientation relationships between phases. To obtain additional insight into microstructure evolution, misorientation-angle distributions obtained in this work were expressed in terms of grain-boundary *density*, i.e., the measured grain-boundary length for a given misorientation angle divided by the area of the EBSD map. From prior experience, this metric provides a direct comparison of grain-boundary characteristics, thus enabling more reliable interpretation of the key physical mechanisms governing microstructure evolution.

[‡]*To remove the artificial martensite which could be introduced during the mechanical polishing, relatively long-term electropolishing (~1 min) was utilized for sample preparation.*

Accepted manuscript

ACCEPTED MANUSCRIPT

Texture data were derived from low-resolution maps; the analyzed area ranged from 1 to 21 mm^2 depending on the particular material condition (supplementary Table S1). However, due to the coarse-grain character of the base material, these maps typically contained a limited number of austenite grains, thus enabling *qualitative* analysis only. Texture calculations were performed assuming orthotropic sample symmetry and employing either a 16^{th}-order harmonic-series-expansion method or a discrete binning approach with a bin size of 5°. In both cases, Gaussian smoothing of 5^o was applied and Bunge convention was utilized for Euler angles.

To establish the effect of cryogenic rolling on mechanical behavior, tension specimens were machined from the base material as well as the cryo-rolled materials. These specimens had a gauge section measuring 15-mm length (RD), 6.7-mm width (TD), and 1.0-mm thickness (ND). Each specimen was pulled to failure at ambient temperature in an Instron 5982 testing machine using a nominal strain rate of 10^{-3} s^{-1}. Two tensile specimens were tested for each material condition.

3. Results

3.1. Broad aspects of strengthening and microstructure evolution

3.1.1. Strengthening behavior

Measurements of the evolution of material strength as function of strain provided indirect insight into microstructural changes during rolling (Fig. 1). As expected, rolling led to significant hardening (Fig. 1a). Specifically, the yield strength increased more than six-fold after 30 pct. reduction (Fig. 1b). The hardening rate $\delta\sigma/\delta e$ (in which $\delta\sigma$ denotes the increase in yield strength for an increment in true strain δe) further quantified the hardening effect (Fig. 1c). The peak hardening rate was noted for the low levels of deformation (i.e., 10-pct. reduction) and then gradually decreased with imposed strain. However, an additional strengthening peak was observed after 30 pct. reduction. In greater details, the underlying strengthening mechanisms are discussed in Section 4.4.

3.1.2. Low-resolution EBSD observations

The broad features of microstructure evolution during rolling were revealed in low-resolution EBSD phase maps (Fig. 2). For simplicity, only selected portions of the acquired maps are shown in the figure. In the maps, austenite, α'-martensite and ε-martensite are colored white, red, and yellow[§], respectively, whereas HABs (as well as phase boundaries) and $\Sigma 3$ misorientations are depicted as black and green lines, respectively; LABs are omitted for clarity. The fractions of the martensitic phases as a function of strain derived from the low-resolution maps are shown in Fig. 3; the analyzed areas are given in supplementary Table S1. Considering the relatively coarse scan step size for these scans (i.e., 1 or 2 μm) as well as the fine scale of the martensitic constituents, the measured contents were likely underestimated.

[§] Here and hereafter, the reader is referred to the online version of this paper to view the figures in color.

Accepted manuscript

ACCEPTED MANUSCRIPT

The original microstructure was dominated by relatively-coarse grains containing annealing twins (Fig. 2a). Rolling to a 5-pct. reduction led to relatively-minor changes at the grain scale (Fig. 2b)[**]. A transformation of the original annealing-twin boundaries within the austenite grains into random boundaries was the only feature of note; an example is indicated by the arrow in Fig. 2b. This effect is well described in the scientific literature [e.g., 40-42] and is usually attributed to strain-induced crystallographic rotations of adjacent twin/matrix material from their original orientations. Almost no evidence of strain-induced martensitic transformations was found at 5-pct. reduction (Fig. 3).

An increase in the rolling reduction to 10 pct. promoted a noticeable amount of martensitic transformation (Figs. 2c & 3). Both α' and ε martensitic phases were found. These phases were interspersed and consisted of two different morphologies (Fig. 2c): (i) series of nearly-parallel bands within prior-austenite grains (circled example) and (ii) relatively-coarse domains resembling the original equiaxed austenite grains. The possible origin of the martensite morphology is discussed in Section 4.2.4. For now, it is worth noting that the fraction of α'-martensite greatly exceeded that of ε-martensite (Fig. 3). Remarkably, the simultaneous presence of both martensitic phases in the studied AISI 321 austenitic stainless steel has been confirmed recently by TEM and X-ray diffraction techniques [43, 44]. This effect was perhaps attributable to relatively low stacking fault energy of this material, i.e., ~20 mJ/m^2 at ambient conditions.

Further increases in reduction to 15 pct. and 23 pct. provided only limited changes in both morphology (Figs. 2c-e) as well as martensite fractions (Fig. 3). However, the additional strain led to an increase in the volume fraction of α'-martensite at the expense of ε-martensite (Fig. 3). This effect may be explained at least partially in terms of an $\varepsilon \rightarrow \alpha'$ phase transformation which is often observed during cold deformation of metastable austenitic alloys [20-26]. An increase in the fraction of $\Sigma 3$ twin boundaries within austenite grains (circled example in Fig. 2f) was also observed. Considering the fine morphology of such twins, this observation likely indicated the activation of mechanical twinning.

Remarkably, no clear evidence of shear banding was found for the entire range of strains investigated here.

3.1.3. High-resolution EBSD observations

Additional insight into microstructural changes was obtained from high-resolution EBSD scans (Fig. 4). To facilitate microstructure interpretation, Kikuchi-band-contrast (image quality) maps were superimposed with the martensitic phases in these figures; moreover, EBSD orientation maps are also given in supplementary Fig. S2. In Kikuchi-band-contrast maps, the sharpness decreases in regions with crystal defects, thus providing images comparable to conventional metallography. In addition to the martensitic phases, LABs, HABs, and $\Sigma 3$ twin

[**] In view of the relatively-low rolling reduction (5 pct.), the elongated grain morphology observed in Fig. 2b was most likely associated with local variations of grain shape in the original microstructure (supplementary Fig. S1).

Accepted manuscript

ACCEPTED MANUSCRIPT

boundaries are indicated in Fig. 4 as blue, black, and green lines, respectively; the traces of several important crystallographic planes are also shown in the maps as dotted lines.

The microstructure of the material rolled to a 5-pct. reduction comprised regular arrays of intersecting bands (Fig. 4a). The dark color of the bands indicated an increased concentration of crystal defects. Such bands, consisting of dislocations and/or stacking faults, are often observed in lightly-deformed low-SFE metals and are termed *deformation bands* throughout the manuscript. The traces of the deformation bands in the present work were typically aligned with 111, 110 or 100 crystallographic planes.

As mentioned in the previous section, a further increase in reduction resulted in martensitic transformations. Of particular interest was the observation that both martensitic phases were concentrated almost exclusively *within* the deformation bands[††] (Figs. 4b-d). This presumably indicated a preferential nucleation of martensite in regions of high strain and agreed with previous reports in the literature [20-22, 24-25, 30]. In addition to the martensitic phases, the bands also contained sporadic nanoscale twins (Figs. 4b-c). Mechanical twinning became particularly pronounced by 30 pct. reduction (Fig. 4d).

Importantly, the deformation bands were rarely outlined by LABs (Fig. 4), thus indicating that the orientation difference between the bands and the austenite matrix was below the EBSD resolution limit (i.e., 2°).

3.2. Microstructure evolution in the austenite phase

The fundamental aspects of microstructure evolution in the *austenite* phase were examined in terms of the development of texture and misorientation distribution.

3.2.1. Texture

Texture evolution in the austenite phase was quantified in terms representative sections ($\varphi_2 = 0°$, $\varphi_2 = 45°$, or $\varphi_2 = 65°$) of orientation distribution functions (ODFs) (Fig. 5). The base material had a very weak crystallographic texture with a peak intensity of ~2.4 times random (Fig. 5a). Nevertheless, some crystallographic preference of a {111}<*uvw*> γ-fiber as well as a {001}<100> Cube texture was noted.

After rolling to relatively-low reductions, the original texture was broken into an irregular pattern (e.g., Fig. 5b for 10-pct. reduction). The development of a distinct rolling texture was found only after 30-pct. reduction (Fig. 5c). To a first approximation, this latter texture comprised the superposition of two partial fibers: a dominant α {110}<*uvw*> and a relatively-weak β (Fig. 5c). Within the α-fiber, strong Goss {110}<100> and Brass {110}<112> components were developed, whereas the β-fiber was dominated by near-Copper {112}<111> and S {123}<634> orientations (Fig. 5c). Generally, the measured texture was broadly similar to that typically observed in moderately-rolled face-centered-cubic metals with low SFE [17, 45].

[††] For the material with a 30-pct.-reduction, a small fraction of martensite was also found within mechanical twins.

Accepted manuscript

ACCEPTED MANUSCRIPT

3.2.2. Misorientation distribution

The effect of rolling reduction on the misorientation-angle and misorientation-axis distributions in austenite is shown in Figs. 6a and 7, respectively. For clarity, the high-angle portion of the misorientation-angle distributions is shown as an insert in the top right corner of Fig. 6a; statistical data derived from the distributions are presented in Figs. 6b-e.

As expected, the microstructure of the annealed base material was dominated by $\Sigma 3$ twin boundaries which produced a sharp peak at 60° in the misorientation-angle distribution (Fig. 6a) and a dense cluster near <111> in the misorientation-axis distribution (Fig. 7a). The 5-pct. reduction led to a small increase in LAB area fraction (Figs. 6a, b) and a marked decrease in the mean LAB misorientation (Fig. 6c). Both these effects presumably originated from the formation of deformation-induced dislocation boundaries. In addition, a slight reduction in the proportion of $\Sigma 3$ twin boundaries was observed (Figs. 6a, b). As mentioned in Section 3.1.2, this behavior can be ascribed to the gradual (strain-induced) transformation of twin boundaries into random HABs. In fact, the measured misorientations of twin boundaries was found to deviate substantially from the ideal twin-matrix orientation relationship (Fig. 6d) and the misorientation axes of the twin boundaries were widely scattered around <111> after 5-pct. reduction (Fig. 7b).

A reduction of 10 or 15 pct. resulted in a marked increase in the proportion of LABs (Figs. 6a, b) thus providing evidence of the extensive development of deformation-induced boundaries. Furthermore, the increase of mean LAB misorientation (Fig. 6c) suggested the progressive evolution of such boundaries, as is normally observed in cold-worked metals due to the operation of the grain subdivision mechanism [e.g. 46]. Remarkably, the misorientation axes of LABs were preferentially clustered near <110> (Figs. 7c, d); the reason for this effect is not clear. On the other hand, twin boundaries almost completely disappeared (Figs. 6a-b), thereby indicating their elimination with relatively small levels of imposed strain (Fig. 6d). An increased fraction of 36^{o}<302> and 44^{o}<115> misorientations was also noted (indicated by the arrows in Figs. 6a and 7c-d, Fig. 6e). These boundaries were typically found within deformation bands (not shown).

A yet further increase in reduction to 30 pct. gave rise to substantial changes, principally a reduction in LAB fraction (Fig. 6b). This effect can be ascribed to the large increase in new $\Sigma 3$ twin boundaries (Fig. 6b) with misorientation very close to that of the ideal $\Sigma 3$ (Fig. 6d). All these observations thus provided evidence of the activation of mechanical twinning, as suggested in Section 3.1.2. On the other hand, the 36^{o}<302> and 44^{o}<115> misorientations disappeared almost completely from the microstructure at the highest rolling reduction (Figs. 6a, 7e-f, and Fig. 6e).

3.3. Microstructure evolution in α'-martensite

Insight into the α' martensitic transformation was obtained by quantifying the orientation relationship with the parent austenite as well as the texture and misorientation distributions within the α' as a function of imposed deformation.

Accepted manuscript

ACCEPTED MANUSCRIPT

3.3.1. Orientation relationship

The orientation relationship between adjacent α'-martensite and parent austenite was established via 111 and 110 pole figures derived from high-resolution EBSD data; typical examples are shown in Fig. 8. For clarity, crystallographic directions in austenite that are close to those in the α'-martensite are circled.

Shortly after initiation of the martensitic transformation (i.e., 10-pct. reduction), the <111> and <110> directions of the austenite were typically found to be very close to the respective <110> and <111> directions of the α'-martensite (Fig. 8a). This correspondence indicated a Kurdjumov-Sachs (K-S) relationship between the phases, viz. $\{111\}_{\gamma}$ || $\{110\}_{\alpha'}$ and $<110>_{\gamma}$ || $<111>_{\alpha'}$, in agreement with numerous reports in the literature [19-20, 23, 27-28, 33].

After rolling to higher reductions, however, the respective directions in the austenite and the α'-martensite were found to deviate substantially from each other (Fig. 8b). These deviations exceeded the EBSD resolution (i.e., 2°) thus probably reflecting a real phenomenon. Considering the significant texture changes in the austenite at higher rolling reductions (Figs. 5b, c), the divergence was likely associated with strain experienced by the austenite and/or α'-martensite following the phase transformation.

3.3.2. Texture

ODF[‡‡] data for various levels of reduction shed more light on the α'-martensitic transformation (Fig. 9). Overall, the ODFs revealed that the texture of the martensitic phase was not random. Shortly after initiation of the martensitic transformation (i.e., after 10-pct. reduction), the ODF was dominated by a (0°; 0°; 0°), i.e., Cube {001}<100>, component (Fig. 8a). A relatively-weak (45°;0°;0°;) component was also present in the ODF (Fig. 8a). By contrast, after 30-pct. reduction, the (45°;0°;0°), i.e., {001}<110> orientation had become dominant, whereas the Cube component had disappeared (Fig. 8b). The development of the {001}<110> texture in the strain-induced martensite has been recently reported by Szpunar, *et al*. [14-15, 38]. This texture component was suggested to originate from the martensitic transformation occurring in austenite grains with a Copper {112}<111> orientation [14].

3.3.3. Misorientation distributions

The reduction dependence of the misorientation-angle and misorientation-axis distributions in the α'-martensite are shown in Figs. 10a and 11, respectively. For clarity, the high-angle portion of the misorientation-angle distributions is shown as an insert in the top right corner of Fig. 10a; statistical data derived from the distributions are presented in Figs. 10b-d.

Shortly after initiation of the martensitic transformation, the misorientation distribution exhibited a very specific form (Figs. 10a and 11a). Assuming that the α'-martensite had undergone limited straining at the low reduction at which it first formed, it can be concluded that the measured misorientations arose from the phase transformation per se and were thus associated with *crystallographic variants*. Due to the crystal symmetry of the γ and α' phases,

[‡‡] For bcc metals, ODF sections of Euler space usually comprise either to φ_1=constant or to φ_2=constant. In this work, the former approach is shown in Fig. 9, whereas the latter sections are given in supplementary Fig. S3.

Accepted manuscript

ACCEPTED MANUSCRIPT

there are 24 possible variants that obey the K-S relation; the misorientations between given pairs of variants are very specific (supplementary Table S2). For a semi-quantitative analysis of the degree of variant selection during the martensitic transformation, inter-variant misorientations are often expressed as those between V1 and other variants (supplementary Table S3). Hence, the relationship between the measured misorientation distribution and variant selection was established from plots of the area fractions of variant boundaries (Figs. 10b-c). At the low reduction at which the α'–martensite formed, the inter-variant boundaries comprised ~50 pct. of the total grain-boundary area (Fig. 10c), thus confirming the transformation origin of the misorientation distribution. In addition, there was a clear preference for V1/V2 and V1/V6 variant boundaries (Fig. 10b), thereby indicating substantial variant selection during the martensitic transformation.

In addition to the inter-variant boundaries, a measurable proportion of 30^{o}<111> and 36^{o}<302> misorientations was also found (indicated by arrows in Figs. 10a and 11a; Fig. 10d). These boundaries were not associated with the K-S orientation relationship; their origin is unknown at present.

In samples deformed to reductions greater than 10 pct., the inter-variant boundary fraction gradually decreased (Figs. 10b-c). The 30°<111> and 36°<302> misorientations also tended to disappear (Figs. 10a, 10d and 11b-d). On the other hand, the proportion of LABs increased significantly (Figs. 10a & c). The possible origin of these observations is discussed in Section 4.3.

It is also worth noting that a 30-pct. reduction led to a large increase in V1/V2, V1/V3 (or V1/V5), V1/V7, and V1/V8 variant boundaries (Fig. 10b). This result is discussed in Section 4.2.3.

3.4. Microstructure evolution in ε-martensite

Microstructure evolution in ε-martensite was quantified via its orientation relationship with austenite and α'-martensite as well as texture and misorientation distributions as function of strain.

3.4.1. Orientation relationship

The orientation relationship between adjacent austenite, ε-martensite, and α'-martensite phases was established via 111, 110, 0001, and $11\bar{2}0$ pole figures derived from high-resolution EBSD data; typical examples are shown in Fig. 12. For clarity, crystallographic directions in austenite and α'-martensite that are close to those in the ε-martensite are circled.

Unfortunately, the orientation relationship between ε-martensite and the other phases was confounded by significant experimental scatter. Very often, no clear relationship between the phases was found (e.g., Fig. 12a). In some cases, on the other hand, a nearly ideal $\{111\}_{\gamma}$ || $\{0001\}_{\varepsilon}$ and $<110>_{\gamma}$ || $<11\text{-}20>_{\varepsilon}$ Shoji-Nishiyama orientation relation was observed between austenite and ε-martensite (e.g., Fig. 12b). In such instances, *all* of the orientation peaks for the ε phase coincided with the corresponding directions in the austenite as indicated in Fig. 12b. This suggests the formation of only *one* specific crystallographic variant of the ε-martensite among

ACCEPTED MANUSCRIPT

four possibilities. That is to say, variant selection was very pronounced. The ε phase in such cases was also related with the α′-martensite via the Burgers orientation relationship, viz. $\{0001\}_{\varepsilon}$ || $\{110\}_{\alpha'}$ and $<11\text{-}20>_{\varepsilon}$ || $<111>_{\alpha'}$, (Fig. 12b). This observation thus provided evidence that the γ→ε→α′ transformation sequence also contributed to the formation of α′-martensite.

3.4.2. Texture

Texture data in the form of 0001 and $11\bar{2}0$ pole figures for two levels of reduction shed more light on the ε-martensite transformation (Fig. 13). Shortly after initiation of the transformation, the ε-martensite was characterized by a distinct texture which can be approximately described as 0001 poles lying at ± 40° to the RD (Fig. 13a). After 30 pct. reduction, however, the texture peaks had moved toward the ND, thus forming 0001 components at ± 25° to the RD (Fig. 13b). Each of these "split" textures was relatively strong with peak intensities of 5 - 10 times random.

The development of similar 0001 components at ± 20° to the RD in ε-martensite during cold rolling of metastable austenitic stainless steel has been reported by Lu, *et al.* [3].

3.4.3. Misorientation distributions

The reduction dependence of the misorientation-angle and misorientation-axis distributions in the ε-martensite are shown in Figs. 14a and 15, respectively; statistical data derived from the distributions are presented in Figs. 14b-c.

Shortly after nucleation, the ε-martensite was characterized by a complex misorientation distribution (Figs. 14a and 15a). Among the preferential misorientations, $86^{o}<11\bar{2}0>$ boundaries were likely attributable to $\{10\bar{1}2\}$ twins [48]; the origin of the other peaks is not clear. Considering the similarity between the crystal structures of ε-martensite and magnesium, the misorientation peaks near 50° and 60° (Figs. 14a and 15a) may be associated with boundaries between crystallographic variants of the $\{10\bar{1}2\}$ twins, whereas $30^{o}<0001>$ boundaries may be attributable to the split-basal texture (Fig. 13a). On the other hand, by analogy with observations for α-titanium, increased proportions of ~ $90^{o}<10\bar{1}0>$ and ~ $93^{o}<16;\bar{4};1\bar{2};3>$ (Figs. 14a and 15a) may originate from $\{11\bar{2}3\}$ twinning and $\{10\bar{1}2\}-\{11\bar{2}3\}$ secondary twinning, respectively. However, this possibility appears less likely due to the marked difference of the *c*/*a* ratio in this material and ε-martensite (1.587 *vs* 1.624). Surprisingly, the misorientation distribution demonstrated no preference for $70.5^{o}<11\bar{2}0>$ boundaries associated with the crystallographic variants of the γ→ε martensitic transformation [49]. This indirectly indicates strong variant selection during transformation in agreement with the remarks in Section 3.4.1.

Rolling to higher reductions resulted in an increase in the fraction of LABs (Fig. 14b) and a decrease in the mean LAB misorientation (Fig. 14c), thereby indicating extensive formation of deformation-induced LABs in ε-martensite. On the other hand, the entire misorientation distribution became relatively smooth (Figs. 14a & 15b-d) and the proportion of $\{10\bar{1}2\}$ twin boundaries was reduced (Fig. 14b) presumably due to strain-induced crystallographic rotations of twins and surrounding matrix, as discussed in Section 3.1.2.

ACCEPTED MANUSCRIPT

4. Discussion

4.1. Grain refinement in austenite

The observed changes in microstructure in the austenite phase were broadly similar to those often observed during cold working of low-SFE metals. Specifically, the early stage of material flow was characterized by deformation banding (Figs. 4a-c), presumably due to dissociation of perfect dislocations into Shockley partials and stacking faults. However, the deformation bands were *not* solely parallel to {111} slip planes, but were often found to be aligned with either {110} or {100} planes (Fig. 4). Assuming a dislocation origin of such bands, their alignment with {110} or {100} may be explained in terms of *interactions* between several different slip systems operating within the same grain. For instance, tangling of dislocations gliding on (111) planes with those on $(11\bar{1})$ planes may result in a deformation band aligned with (110) planes. On the other hand, the interaction of (111) and $(1\bar{1}\,\bar{1})$ dislocations may give rise to deformation bands along (100) planes. If so, the deformation bands may not have been slip bands but were rather dislocation walls (or LABs).

Increased rolling reduction led to the formation of extensive deformation-induced LABs (Figs. 6a-b). However, their mean misorientation increased relatively slowly (Fig. 6c), and almost no LAB-to-HAB transformation was observed. This was likely due to martensitic transformations within the deformation bands (i.e., the most-heavily deformed areas) which suppressed the progressive development of deformation-induced boundaries. Thus, the strain-induced martensitic transformation inhibited grain-refinement in the austenitic phase via the normal grain-subdivision mechanism. On the other hand, mechanical twinning appeared to be the dominant mechanism controlling HAB formation in austenite. As expected, this mechanism was activated only after moderately-high rolling strains (~30 pct. reduction, Fig. 6b), which presumably provided the necessary level of stress.

In addition to twinning, strain-induced 35^{o}<302> and 44^{o}<115> misorientations also contributed somewhat to the development of HABs in the austenitic phase (Fig. 6e). Considering a preferential concentration of such boundaries within deformation bands, they probably originated from an interplay between stacking faults, but this conjecture requires further study.

4.2. Martensitic transformations

4.2.1. Transformation path

Per the results in Fig. 3, the early stages of straining were characterized by both $\gamma \rightarrow \alpha'$ as well as $\gamma \rightarrow \varepsilon$ martensitic reactions, albeit the former sequence seemed to dominate. The decrease in the fraction of the ε-martensite at higher strains (Fig. 3) was most likely attributable to the $\varepsilon \rightarrow \alpha'$ transformation. Therefore, both $\gamma \rightarrow \alpha'$ and $\gamma \rightarrow \varepsilon \rightarrow \alpha'$ sequences contributed to the development α' martensite. However, the mutual contributions of these two mechanisms are unclear.

ACCEPTED MANUSCRIPT

4.2.2. Effect of crystallographic orientation of parent austenite on martensite formation

As mentioned in Section 3.1.3, the strain-induced martensite nucleated almost exclusively within deformation bands (Figs. 4b-d). If so, the martensitic reactions should be closely related with the underlying slip systems in austenite. This implies a sensitivity of this process to *crystallographic orientation* of austenite grains [51-54]. Specifically, it has been shown recently that ε-martensite develops preferentially in austenite grains with Copper {112}<111> and S {123}<634> orientations, and this results in the development of a texture characterized by 0001 poles at ± 20^{o} to the RD in the ε phase [3].

To examine this possibility for the α′ transformation, several high-resolution EBSD maps were obtained for α′ martensite domains with crystallographic orientations close to the dominant texture components, i.e., either (0°;0°;0°) or (45°;0°;0°;). A nearly-perfect K-S orientation relationship between the α′ martensite and the remnants of the parent austenite was confirmed. In addition, the orientations of the parent austenite grains were derived from such maps (Fig. 16). It is apparent that the (0°;0°;0°) orientation of α′ martensite originated from the (0°;45°;0°) Goss orientation of austenite (Fig. 16a). In terms of Miller indices, this means that the Cube {001}<100> orientation of α′ martensite originated from the {110}<100> orientation of austenite. On the other hand, the (45°;0°;0°;) orientation of α′ martensite was produced by austenite grains with an orientation close to Brass (35°;45°;0°) (Fig. 16b). In terms of Miller indices, this means that the {001}<110> orientation of α′ martensite originated from the {110}<112> orientation of austenite. The K-S orientation relationship between the Brass orientation in austenite and (45°;0°;0°) orientation in α′ martensite has been also recently reported by Souza Filho, *et al.* [55].

It can thus be concluded that α′ martensitic transformation at relatively low strains developed primarily in austenite grains with near-Goss orientations. However, the formation of deformation texture in austenite after 30 pct. reduction (Fig. 5c) and the concomitant change in slip activity resulted in preferential martensitic reaction in austenite grains with a Brass orientation. However, the fundamental reason(s) for preferential α′ martensitic transformation in austenite grains with Goss and Brass orientations warrants further research.

It should be noted that the {100}<110> orientation is also known to originate from rolling of body-centered-cubic metals, i.e., it may be related to *deformation* of the α′ martensite. Therefore, the origin of this textural component warrants further study.

4.2.3. Variant selection

The close relationship between the martensitic transformations and the operative austenite slip systems mentioned above suggests noticeable variant selection [51, 53], which was indeed observed in the present work (Sections 3.3 and 3.4). This effect was particularly pronounced for ε-martensite, as shown by direct crystallographic measurements (Fig. 12b), the formation of a relatively-sharp texture (Fig. 12a), and the variant-less character of the misorientation distribution (Figs. 14a and 15a) in this phase.

In the context of the discussion in the previous section, the observed redistribution of inter-variant misorientations in α′ martensite after 30 pct. reduction (Fig. 10b) may be attributed

ACCEPTED MANUSCRIPT

to the development of near-Brass texture in austenite and the resulting re-activation of the martensitic transformation.

The sensitivity of the martensitic transformations to crystallographic orientation of austenite grains as well as the marked variant selection governing this process resulted in the development of relatively-strong textures in both martensitic phases (Figs. 9 & 13).

4.2.4. Martensite morphology

Due to the preponderance of martensitic formation within deformation bands, the resulting phases can likely be characterized as lamellar in morphology. However, because of the arbitrary orientation of the martensite platelets relative to the section plane (i.e, stereological effects), their appearance might vary from a series of narrow bands to relatively-coarse grain-shaped domains. This was indeed observed in low-resolution EBSD maps (Figs. 2b-d).

Considering the limited volume fraction of deformation bands, the martensitic reaction should eventually have reached a saturation. This was also observed for the deformation range comprising 10 to 23 pct. rolling reduction (Fig. 3). On the other hand, the formation of Brass texture in moderately-rolled austenite (Fig. 5c) and the concomitant activation of new deformation bands should re-activate the martensitic transformation, as mentioned above. This effect, together with the $\varepsilon \rightarrow \alpha'$ transformation, promoted an increase of α' proportion after 30 pct. rolling (Fig. 3).

4.3. Deformation-induced changes in martensite

As mentioned in Section 3.1.2, the applied strain may transform twin boundaries into random grain boundaries. Therefore, the twin boundaries as well as any other specific misorientations, can serve as indicators of local strain. In this context, the elimination of the unusual 30°<111> and 36°<302> misorientations in α'-martensite as well as the smoothing of the misorientation distribution in ε-martensite during rolling (Figs. 10d and 14a, respectively) provide evidence that both martensitic phases underwent some plastic strain. This conclusion was also supported by the gradual increase in LAB density (Figs. 10a and 14a) and LAB fraction (Figs. 10c and 14b) as well the disruption of the ideal orientation relationships between the martensitic phases and austenite (Figs. 8b and 12a). The latter effect was most pronounced for ε-martensite, thus suggesting that this phase experienced a relatively-large strain. The noticeable strain experienced by the ε phase during cold working has been recently reported by Lu, *et al.* [3] and Souza Filho, *et al.* [55].

4.4. Strain hardening

On the basis of the detailed EBSD characterization of microstructure changes in previous sections, the strain hardening mechanisms can be deduced. Per Figs. 1a-b, a 5-pct.-reduction nearly doubled material strength. Microstructural observations in this material condition revealed only a minor increase in LAB density and virtually no martensitic transformations (Figs. 6a-b and 3, respectively); therefore, the very large strengthening effect was presumably attributable to dislocation hardening and/or deformation banding (Fig. 4a).

ACCEPTED MANUSCRIPT

Rolling to a 10-pct. reduction provided the highest strengthening rate (Fig. 1c). This phenomenon was associated with strain-induced martensitic transformations (Fig. 3). In addition, a substantial increase in the LAB area in the austenite phase (Figs. 6a-b) also contributed perhaps to strengthening some extent. The considerable decrease in hardening rate in the range of 10 to 23 pct. reduction (Fig. 1c) was most likely due to the saturation of martensite content (Fig. 3), as discussed in Section 4.2.4. In this strain interval, work hardening is thought to arise primarily from sub-boundary strengthening in austenite (Figs. 6a-b) and strain hardening of the martensitic phases, as suggested in previous sections.

The enhancement of the strengthening rate after 30 pct. reduction presumably originated from a further increase in α' martensite volume fraction (Fig. 3) due to $\varepsilon \rightarrow \alpha'$ transformation as well as the development of a Brass texture in austenite as discussed in Section 4.2.4.

5. Conclusions

EBSD was applied to quantify microstructure evolution during cryogenic rolling of type 321 metastable austenitic stainless steel for thickness reductions between 5 and 30 pct. Based on detailed microstructural characterization, the microstructure dependence of strength was elucidated. The main conclusions from this work are as follows.

1. Microstructure evolution in the austenite phase is broadly similar to that normally observed during cold working of cubic metals with low-SFE. Specifically, it is characterized by extensive deformation banding, formation of poorly developed LABs, and activation of mechanical twinning after a moderate degree of reduction.

2. As expected, cryogenic rolling induces a martensitic transformation. The martensite nucleates almost exclusively within deformation bands, i.e., the most-highly strained areas in the austenite phase. This prevents the continued development of deformation-induced boundaries in austenite and thus inhibits grain-refinement of this phase via the normal grain-subdivision process. Mechanical twinning is thus the sole source for HAB formation in austenitic phase at high strains.

3. Evidence of two transformation sequences, viz., $\gamma \rightarrow \alpha'$ and $\gamma \rightarrow \varepsilon \rightarrow \alpha'$, are observed; the former one predominates. Both transformation paths follow the general orientation relations $\{111\}_{\gamma} \parallel \{0001\}_{\varepsilon} \parallel \{110\}_{\alpha'}$ and $\langle 110 \rangle_{\gamma} \parallel \langle 11\text{-}20 \rangle_{\varepsilon} \parallel \langle 111 \rangle_{\alpha'}$ but are gradually destroyed with additional strain.

4. The occurrence of strain-induced martensitic phases within deformation bands implies a close relationship between the transformation processes and slip activity in the parent austenite grains. Specifically, the martensite reactions occur preferentially in austenite grains with crystallographic orientations close to Goss {110}<100> and Brass {110}<112>. Moreover, the martensitic transformations are governed by strong/preferential variant selection which is most marked for the formation of ε-martensite. The sensitivity of the martensitic reactions to the crystallographic orientation of austenite as well as strong variant selection occurring during this process results in sharp crystallographic textures in both martensitic phases.

Accepted manuscript

ACCEPTED MANUSCRIPT

5. The preferential development of both martensitic phases within deformation bands results in rapid saturation of martensite evolution thus giving rise to its near-sigmoid dependence on strain. However, the development of a deformation-induced Brass texture in austenite and the concomitant activation of new deformation bands re-activates the martensitic transformation.

6. Both martensitic phases experience plastic strain during rolling.

7. Cryogenic rolling imparts dramatic strengthening resulting in a more than six-fold increase in yield strength for 321 stainless steel. The strain hardening is mostly due to the martensitic transformations. However, dislocation- as well as LAB hardening also provide some contribution to material strength.

Acknowledgements

Financial support from the Russian Fund for Fundamental Research (project No.17-42-020426) is gratefully acknowledged. The authors also thank P. Klassman for technical assistance during cryogenic rolling.

Declarations of interest: none

Data availability

The raw/processed data required to reproduce these findings cannot be shared at this time due to technical or time limitations

References

[1] K. Tomimura, S. Takaki, S. Tanimoto, Y. Tokunaga, Optimal chemical composition in Fe-Cr-Ni alloys for ultra grain refining by reversion from deformation induced martensite, ISIJ International 31 (1991) 721-727

[2] K. Tomimura, S. Takaki, Y. Tokunaga, Reversion mechanism from deformation induced martensite to austenite in metastable austenitic stainless steels, ISIJ International 31 (1991) 1431-1437

[3] Y. Lu, B. Hutchinson, D.A. Molodov, G. Gottstein, Effect of deformation and annealing on the formation and reversion of ε-martensite in an Fe–Mn–C alloy, Acta Materialia 58 (2010) 3079–3090, https://doi.org/10.1016/j.actamat.2010.01.045

[4] B. Ravi Kumar, A.K. Singh, B. Mahato, P.K. De, N.R. Bandyopadhyay, D.K. Bhattacharya, Deformation-induced transformation textures in metastable austenitic stainless steel, Mater. Sci. Eng. A429 (2006) 205–211, dx.doi.org/10.1016/j.msea.2006.05.107

[5] M. Eskandari, A. Najafizadeh, A. Kermanpur, Effect of strain-induced martensite on the formation of nanocrystalline 316L stainless steel after cold rolling and annealing, Mater. Sci. Eng. A519 (2009) 46–50, dx.doi.org/10.1016/j.msea.2009.04.038

Accepted manuscript

ACCEPTED MANUSCRIPT

[6] S. Rajasekhara, L.P. Karjalainen, A. Kyröläinen, P.J. Ferreira, Microstructure evolution in nano/submicron grained AISI 301LN stainless steel, Mater. Sci. Eng. A527 (2010) 1986–1996, dx.doi.org/10.1016/j.msea.2009.11.037

[7] R.D.K. Misra, Z. Zhang, P.K.C. Venkatasurya, M.C. Somani, L.P. Karjalainen, Martensite shear phase reversion-induced nanograined/ultrafine-grained Fe–16Cr–10Ni alloy: The effect of interstitial alloying elements and degree of austenite stability on phase reversion, Mater. Sci. Eng. A527 (2010) 7779-7792, dx.doi.org/10.1016/j.msea.2010.08.051

[8] A. Kisko, A.S. Hamada, J. Talonen, D. Porter, L.P. Karjalainen, Effects of reversion and recrystallization on microstructure and mechanical properties of Nb-alloyed low-Ni high-Mn austenitic stainless steels, Mater. Sci. Eng. A657 (2016) 359-370, http://dx.doi.org/10.1016/j.msea.2016.01.093

[9] M. Odnobokova, A. Belyakov, N. Enikeev, D.A. Molodov, R. Kaibyshev, Annealing behavior of a 304L stainless steel processed by large strain cold and warm rolling, Mater. Sci. Eng. A689 (2017) 370-383, http://dx.doi.org/10.1016/j.msea.2017.02.073

[10] G.S. Sun, L.X. Du, J. Hu, R.D.K. Misra, Microstructural evolution and recrystallization behavior of cold rolled austenitic stainless steel with dual phase microstructure during isothermal annealing, Mater. Sci. Eng. A709 (2018) 254-264, http://dx.doi.org/10.1016/j.msea.2017.10.054

[11] D.L. Johannsen, A. Kyrolainen, P.J. Ferreira, Influence of annealing treatment on the formation of nano/submicron grain size in AISI 301 austenitic stainless steels, Metall. Mater. Trans. 37A (2006) 2325-2338.

[12] S. Rajasekhara, P.J. Ferreira, L.P. Karjalainen, A. Kyrolainen, Hall–Petch behavior in ultra-fine-grained AISI 301LN stainless steel, Metall. Mater. Trans. 38A (2007) 1202-1210.

[13] M.C. Somani, P. Juntunen, L.P. Karjalainen, R.D.K. Misra, A. Kyrolainen, Enhanced mechanical properties through reversion in metastable austenitic stainless steels, Metall. Mater. Trans. 40A (2009) 729-744.

[14] M. Nezakat, H. Akhiani, M. Hoseini, J. Szpunar, Effect of thermo-mechanical processing on texture evolution in austenitic stainless steel 316L, Mater. Character. 98 (2014) 10–17, http://dx.doi.org/10.1016/j.matchar.2014.10.006

[15] M. Nezakat, H. Akhiani, S.M. Sabet, J. Szpunar, Electron backscatter and X-ray diffraction studies on the deformation and annealing textures of austenitic stainless steel 310S, Mater. Character. 123 (2017) 115–127, http://dx.doi.org/10.1016/j.matchar.2016.11.019

[16] L.J. Teutonico, The dissociation of dislocations in the face-centered cubic structure, Acta Metall. 11 (1963) 1283-1289, https://doi.org/10.1016/0001-6160(63)90023-3

[17] J. Hirsch, K. Lucke, M. Hatherly, Mechanism of deformation and development of rolling textures in polycrystalline F.C.C. metals – III. The influence of slip inhomogeneities and twinning, Acta Metall. 36 (1988) 2905-2927, https://doi.org/10.1016/0001-6160(88)90174-5

[18] J.W. Christian, S. Mahajan, Deformation twinning, Prog. Mater. Sci. 39 (1995) 1-157, https://doi.org/10.1016/0079-6425(94)00007-7

Accepted manuscript

ACCEPTED MANUSCRIPT

[19] J.W. Brooks, M.H. Loretto, R.E. Smallman, Direct observations of martensite nuclei in stainless steel, Acta Metall. 27 (1979) 1839-1847, https://doi.org/10.1016/0001-6160(79)90074-9

[20] K.H. Lo, C.H. Shek, J.K.L. Lai, Recent developments in stainless steels, Mater. Sci. Eng. R 65 (2009) 39–104, https://doi.org/10.1016/j.mser.2009.03.001

[21] G.B. Olson, M. Cohen, Kinetics of strain-induced martensitic nucleation, Metall. Trans. 6A (1975) 791-795, https://doi.org/10.1007/BF02672301

[22] A.K. De, D.C. Murdock, M.C. Mataya, J.G. Speer, D.K. Matlock, Quantitative measurement of deformation-induced martensite on 304 stainless steel by X-ray diffraction, Scripta Mater. 50 (2004) 1445-1449, https://doi.org/10.1016/j.scriptamat.2004.03.011

[23] T.-H. Lee, E. Shin, C.-S. Oh, H.-Y. Ha, S.-J. Kim, Correlation between stacking fault energy and deformation microstructure in high-interstitial-alloyed austenitic steels, Acta Mater. 58 (2010) 3173–3186, https://doi.org/10.1016/j.actamat.2010.01.056

[24] A. Das, S. Sivaprasad, P.C. Chakraborti, S. Tarafder, Morphologies and characteristics of deformation induced martensite during low cycle fatigue behavior of austenitic stainless steel, Mater. Sci. Eng. A528 (2011) 7909-7914, https://doi.org/10.1016/j.msea.2011.07.011

[25] Y.F. Shen, X.X. Li, X. Sun, Y.D. Wang, L. Zuo, Twinning and martensite in a 304 austenitic stainless steel, Mater. Sci. Eng. A552 (2012) 514-522, https://doi.org/10.1016/j.msea.2012.05.080

[26] P. Mallick, N.K. Tewary, S.K. Ghosh, P.P. Chattopadhyay, Effect of cryogenic deformation on microstructure and mechanical properties of 304 austenitic stainless steel, Mater. Character. (2018), in press, https://doi.org/10.1016/j.matchar.2017.09.027

[27] T. Suzuki, J. Kojima, K. Suzuki, T. Hashimito, M. Ichihara, An experimental study of the martensite nucleation and growth in 18/8 stainless steel, Acta Metall. 25 (1977) 1151-1162, https://doi.org/10.1016/0001-6160(77)90202-4

[28] N. Nakada, H. Ito, Y. Matsuoka, T. Tsuchiyama, S. Takaki, Deformation-induced martensitic transformation behavior in cold-rolled and cold-drawn type 316 stainless steels, Acta Mater. 58 (2010) 895–903, https://doi.org/10.1016/j.actamat.2009.10.004

[29] I. Shakhova, V. Dudko, A. Belyakov, K. Tsuzaki, R. Kaibyshev, Effect of large strain rolling and subsequent annealing on microstructure and mechanical properties of an austenitic stainless steel, Mater. Sci. Eng. A545 (2012) 176-186, https://doi.org/10.1016/j.msea.2012.02.101

[30] S. Sabooni, F. Karimzadeh, M.H. Enayati, A.H.W. Ngan, The role of martensitic transformation on bimodal grain structure in ultrafine grained AISI 304L stainless steel, Mater. Sci. Eng. A636 (2015) 221-230, https://doi.org/10.1016/j.msea.2015.03.101

[31] L. Bracke, K. Verbeken, L. Kestens, J. Penning, Microstructure and texture evolution during cold rolling and annealing of a high Mn TWIP steel, Acta Mater. 57 (2009) 1512–1524, https://doi.org/10.1016/j.actamat.2008.11.036

Accepted manuscript

[32] B. Roy, R. Kumar, J. Das, Effect of cryorolling on the microstructure and tensile properties of bulk nano-austenitic stainless steel, Mater. Sci. Eng. A631 (2015) 241-247, https://doi.org/10.1016/j.msea.2015.02.050

[33] T.S. Wang, J.P. Peng, Y.W. Gao, F.C. Zhang, T.F. Jing, Microstructure of 1Cr18Ni9Ti stainless steel by cryogenic compression deformation and annealing, Mater. Sci. Eng. A407 (2005) 84-88, https://doi.org/10.1016/j.msea.2005.06.022

[34] M. Eskandari, A. Kermanpur, and A. Najafizadeh, Formation of nanocrystalline structure in 301 stainless steel produced by martensite treatment, Metall. Mater. Trans. 40A (2009) 2241-2249, https://doi.org/10.1007/s11661-009-9916-z

[35] T.-H. Lee, C.-S. Oh, S.J. Kim, S. Takaki, Deformation twinning in high-nitrogen austenitic stainless steel, Acta Mater. 55 (2007) 3649-3662, https://doi.org/10.1016/j.actamat.2007.02.023

[36] M. Klimova, S. Zherebtsov, N. Stepanov, G. Salishchev, D.A. Molodov, Microstructure and texture evolution of a high manganese TWIP steel during cryo-rolling, Mater. Character. 132 (2017) 20-30, https://doi.org/10.1016/j.matchar.2017.07.043

[37] A.A. Tiamiyu, J.A. Szpunar, A.G. Odeshi, I. Oguocha, M. Eskandari, Development of ultra-fine-grained structure in AISI 321 austenitic stainless steel, Metall. Mater. Trans. 48A (2017) 5990-6012, https://doi.org/10.1007/s11661-017-4361-x

[38] A.A. Tiamiyu, A.G. Odeshi, J.A. Szpunar, Austenitic reversion of cryo-rolled Ti-stabilized austenitic stainless steel; high resolution EBSD investigation, JMEPEG 27 (2018) 889-904, https://doi.org/10.1007/s11665-018-3180-6

[39] A. Stormvinter, G. Miyamoto, T. Furuhara, P. Hedstrom, A. Borgenstam, Effect of carbon content on variant pairing of martensite in Fe-C alloys, Acta Mater. 60 (2012) 7265-7274, http://dx.doi.org/10.1016/j.actamat.2012.09.046

[40] G. Salishchev, S. Mironov, S. Zherebtsov, A. Belyakov, Changes in misorientations of grain boundaries in titanium during deformation, Mater. Character. 61 (2010) 732-739, https://doi.org/10.1016/j.matchar.2010.04.005

[41] S. Mironov, Y.S. Sato, H. Kokawa, H. Inoue, S. Tsuge, Structural response of superaustenitic stainless steel to friction stir welding, Acta Mater. 59 (2011) 5472-5481, https://doi.org/10.1016/j.actamat.2011.05.021

[42] S. Mironov, K. Inagaki, Y.S. Sato, H. Kokawa, Development of grain structure during friction-stir welding of Cu–30Zn brass, Phil. Mag. 94 (2014) 3137-3147, https://doi.org/10.1080/14786435.2014.951712

[43] M.A. Vasylyev, B.N. Mordyuk, S.I. Sidorenko, S.M. Voloshko, A.P. Burmak, Influence of microstructural features and deformation-induced martensite on hardening of stainless steel by cryogenic ultrasonic impact treatment, Surf. Coat. Technol. 343 (2018) 57-68; https://doi.org/10.1016/j.surfcoat.2017.11.019

[44] B.N. Mordyuk, Y.V. Milman, M.O. Lefimov, G.I. Prokopenko, V.V. Silberschmid, M.I. Danylenko, A.V. Kotko, Characterization of ultrasonically peened and laser-shock peened

Accepted manuscript

ACCEPTED MANUSCRIPT

surface layers of AISI 321 stainless steel, Surf. Coat. Technol. 202 (2008) 4875-4883; https://doi.org/10.1016/j.surfcoat.2008.04.080

[45] J. Hirsch, K. Lucke, Mechanism of deformation and development of rolling textures in polycrystalline F.C.C. metals – I. Description of rolling texture development in homogeneous CuZn alloys, Acta Metall. 36 (1988) 2863-2882, https://doi.org/10.1016/0001-6160(88)90172-1

[46] N. Hansen, D.J. Jensen, Development of microstructure in FCC metals during cold work, Phil. Trans. R. Soc. Lond. A 357 (1999) 1447-1469; doi:10.1098/rsta.1999.0384

[47] B. Sonderegger, S. Mitsche, H. Cerjak, Martensite laths in creep resistant matrtensite 9-12% Cr steels – calculation and measurement of misorientations, Mater. Character. 58 (2007) 874-882, doi:10.1016/j.matchar.2006.08.014

[48] X. Zhang, T. Sawaguchi, Twinning of deformation-induced ε-martensite in Fe-30Mn-6Si shape memory alloy, Acta Mater. 143 (2018) 237-247, https://doi.org/10.1016/j.actamat.2017.10.009

[49] J.H. Yang, C.M. Wayman, On secondary variants formed at intersections of ε martensite variants, Acta Metall. Mater. 40 (1992) 2011-2023, https://doi.org/10.1016/0956-7151(92)90187-J

[50] S.T. Pisarik, D.C. Van Aken, Crystallographic orientation of $\varepsilon \rightarrow \alpha'$ martensite (athermal) transformation in FeMnAlSi steel, Metal. Mater. Trans. 45A (2014) 3173-3177, https://doi.org/10.1007/s11661-014-2303-4

[51] N. Gey, B. Petit, M. Humbert, Electron backscattered diffraction study of ε/α' martensitic variants induced by plastic deformation in 304 stainless steel, Metall. Mater. Trans. 36A (2005) 3291-3299, https://doi.org/10.1007/s11661-005-0003-9

[52] W. Tasaki, K. Tsuchiya, T. Sawaguchi, S. Takamori, Comparison of reverse transformation behaviors of thermally- and deformation-induced ε-martensite in Fe-28Mn-6Si-5Cr shape memory alloy, Mater. Trans. 57(10) (2016) 1707-1713, http://dx.doi.org/10.2320/matertrans.MAW201607

[53] M. Humbert, B. Petit, B. Bolle, N. Gey, Analysis of the $\gamma–\varepsilon–\alpha'$ variant selection induced by 10% plastic deformation in 304 stainless steel at −60°C, Mater. Sci. Eng. A454–455 (2007) 508–517, dx.doi.org/10.1016/j.msea.2006.11.112

[54] C. Ullrich, R. Eckner, L. Krüger, S. Martin, V. Klemm, D. Rafaja, Interplay of microstructure defects in austenitic steel with medium stacking fault energy, Mater. Sci. Eng. A649 (2016) 390-399, http://dx.doi.org/10.1016/j.msea.2015.10.021

[55] I.R. Souza Filho, K.D. Zilnyk, M.J.R. Sandim, R.E. Bolmaro, H.R.Z. Sandim, Strain partitioning and texture evolution during cold rolling of AISI 201 austenitic stainless steel, Mater. Sci. Eng. A702 (2017) 161-172, http://dx.doi.org/10.1016/j.msea.2017.07.010

Accepted manuscript

ACCEPTED MANUSCRIPT

Figure Captions

Figure 1. Effect of rolling reduction on (a) engineering stress-strain curves, (b) yield strength, and (c) hardening rate

Figure 2. Selected portions of low-resolution EBSD phase maps showing (a) original microstructure and its evolution after a rolling reduction of (b) 5 pct., (c) 10 pct., (d) 15 pct., (e) 23 pct., or (d) 30 pct. The scale bar and phase color codes for all maps are given in (a). High-angle (or phase) boundaries are shown as black lines and $\Sigma 3$ boundaries are shown as green lines. RD, TD and ND denote the rolling, transverse, and normal direction, respectively.

Figure 3. Effect of rolling reduction on the volume fraction of the martensitic phases

Figure 4. Selected portions of high-resolution EBSD Kikuchi-band-contrast maps showing the microstructures developed during a rolling reduction of (a) 5 pct., (b) 10 pct., (c) 15 pct., or (d) 30 pct. The color codes for the martensitic phases are given in the top right corner of (a). In the maps, low-angle boundaries are depicted as blue lines, high-angle (or phase) boundaries as black lines, and $\Sigma 3$ boundaries as green lines. The dotted lines indicate the traces of 111, 110 and 100 planes which are closest to the corresponding deformation-band trace

Figure 5. Selected sections ($\varphi_2 = 0°$, $\varphi_2 = 45°$, or $\varphi_2 = 65°$) of orientation distribution functions (ODFs) showing the texture in the *austenite* (a) in the base-metal condition, (b) after 10 pct. reduction (i.e. shortly after initiation of the martensitic transformation), or (c) after 30 pct. reduction. For comparative purposes, several ideal rolling orientations are superimposed on the ODFs

Figure 6. Misorientation measurements in the *austenite* phase as a function of rolling reduction: (a) Misorientation-angle distributions, (b) area fractions of LABs and $\Sigma 3$ twin boundaries, (c) mean LAB misorientation, (d) mean deviation of twin-boundary misorientations from ideal $\Sigma 3$, and (e) area fractions of 36^{o}<302> and 44^{o}<115> misorientations. In (a), the insert in the top right corner shows an enlargement of the high-angle section of the misorientation distributions

Figure 7. Effect of rolling reduction on misorientation-axis distribution in the *austenite* phase in (a) the base material or after a rolling reduction of (b) 5 pct., (c) 10 pct., (d) 15 pct., (e) 23 pct., or (f) 30 pct.

Figure 8. Typical examples showing the local orientation relationship between austenite and α' martensite as function of rolling reduction: (a) 10 pct. (i.e., shortly after initiation of martensitic transformation) or (b) 30 pct. In the pole figures, the closest related directions in the austenite and the α' martensite are circled

Figure 9. ODFs showing the texture in *α' martensite* as function of rolling reduction: (a) 10 pct. (i.e., shortly after initiation of martensitic transformation) or (b) 30 pct.

Accepted manuscript

Figure 10. Misorientation measurements in *α′ martensite* as a function of rolling reduction: (a) misorientation-angle distributions, (b) variant-pairing frequency diagram according to the Kurdjumov-Sachs (K-S) orientation relationship, (c) area fractions of LABs and inter-variant boundaries, and (d) 30^{o}<111> and 36^{o}<302> misorientations. In (a), the insert in the top right corner shows an enlargement of the high-angle section of the misorientation distribution

Figure 11. Effect of rolling reduction on misorientation-axis distribution in *α′-martensite* after a reduction of: (a) 10 pct., (b) 15 pct., (c) 23 pct., or (d) 30 pct.

Figure 12. Typical examples showing the local orientation relationship between austenite, ε martensite, and α′ martensite: (a) the lack of a clear orientation relationship between the austenite and ε martensite, and (b) a nearly-ideal Shoji-Nishiyama orientation relationship between the austenite and ε martensite. In the pole figures, the closest related directions in the austenite, ε martensite, and α′ martensite are circled. In (a), the data were taken after 10-pct. reduction (i.e. shortly after initiation of the martensitic transformation), whereas the data in (b) were obtained from the material subjected to 30-pct. reduction

Figure 13. 0001 and 11-20 pole figures showing the texture in *ε-martensite* as function of rolling reduction: (a) 10 pct. (i.e., shortly after initiation of the martensitic transformation) or (b) 30 pct.

Figure 14. Misorientation measurements in *ε-martensite* as a function of rolling reduction: (a) misorientation-angle distributions, (b) area fractions of LABs and {1012} twin boundaries, and (c) mean LAB misorientation

Figure 15. Effect of rolling reduction on misorientation-axis distribution in *ε-martensite* after a reduction of (a) 10 pct., (b) 15 pct., (c) 23 pct., or (d) 30 pct.

Figure 16. Selected sections (φ_2 = 0° and φ_2 = 45°) of ODFs illustrating the orientation relationship between α′ martensite and austenite measured in the martensite domain with a crystallographic orientation close to (a) (0°; 0°; 0°) or (b) (45^{o};0°;0°). In both cases, the orientation data were taken from material rolled to a 30-pct. reduction. Note: Subtle secondary texture components are also present in the austenitic and martensitic phases in both cases.

Accepted manuscript

Table 1. Nominal chemical composition of program material (wt%) according to Russian industrial standard

Fe	C	Cr	Ni	Mn	Ti	Si	Cu	S	P
Balance	≤0.12	17-19	9-10	≤2.0	0.4-1.0	≤0.8	≤0.3	≤0.02	≤0.035

ACCEPTED MANUSCRIPT

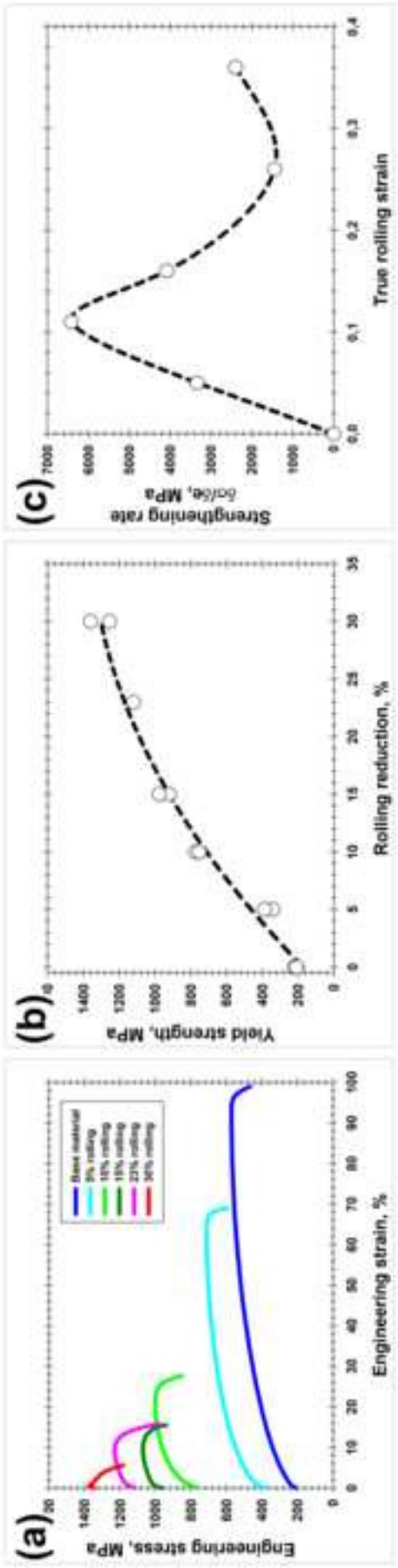


Figure 1. Effect of rolling strain on (a) engineering stress-strain curves, (b) yield strength and (c) strengthening rate.

Figure(s)

Figure(s)

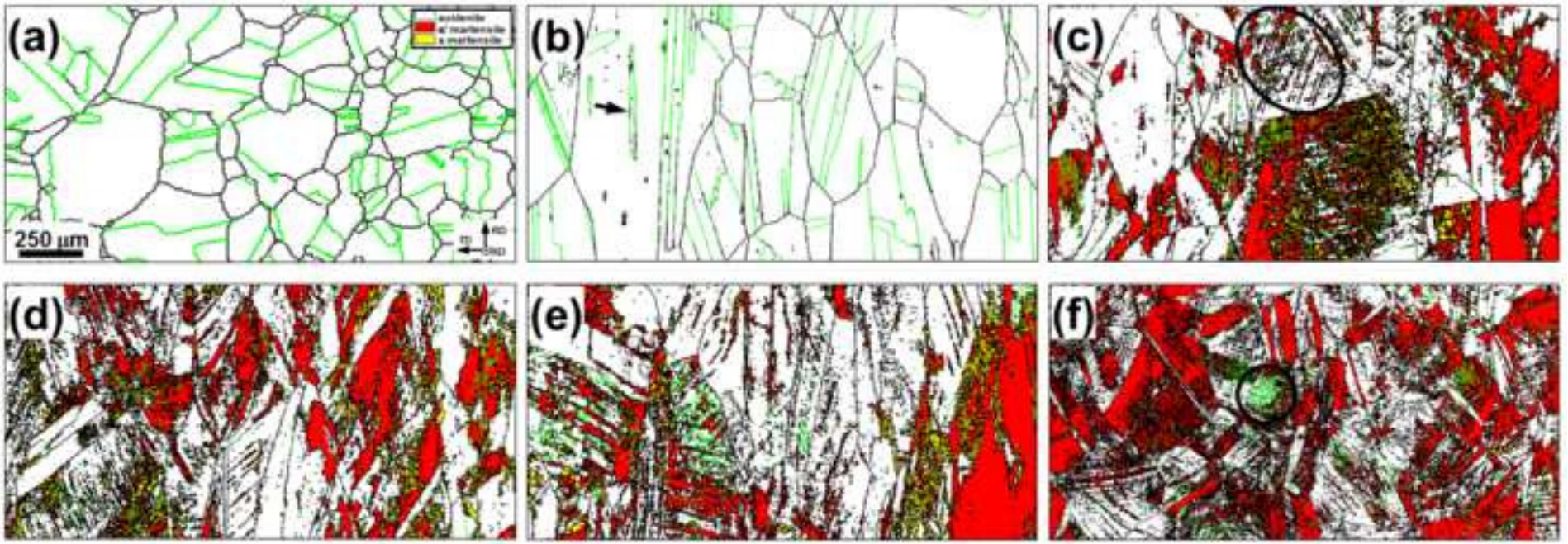


Figure 2. Selected portions of low-resolution EBSD phase maps showing (a) original microstructure and its evolution after a rolling reduction of (b) 5 pct., (c) 10 pct., (d) 15 pct., (e) 23 pct., or (d) 30 pct. The scale bar and phase color codes for all maps are given in (a). High-angle (or phase) boundaries are shown as black lines and Σ3 boundaries are shown as green lines. RD, TD and ND denote the rolling, transverse, and normal direction, respectively.

ACCEPTED MANUSCRIPT

Figure(s)

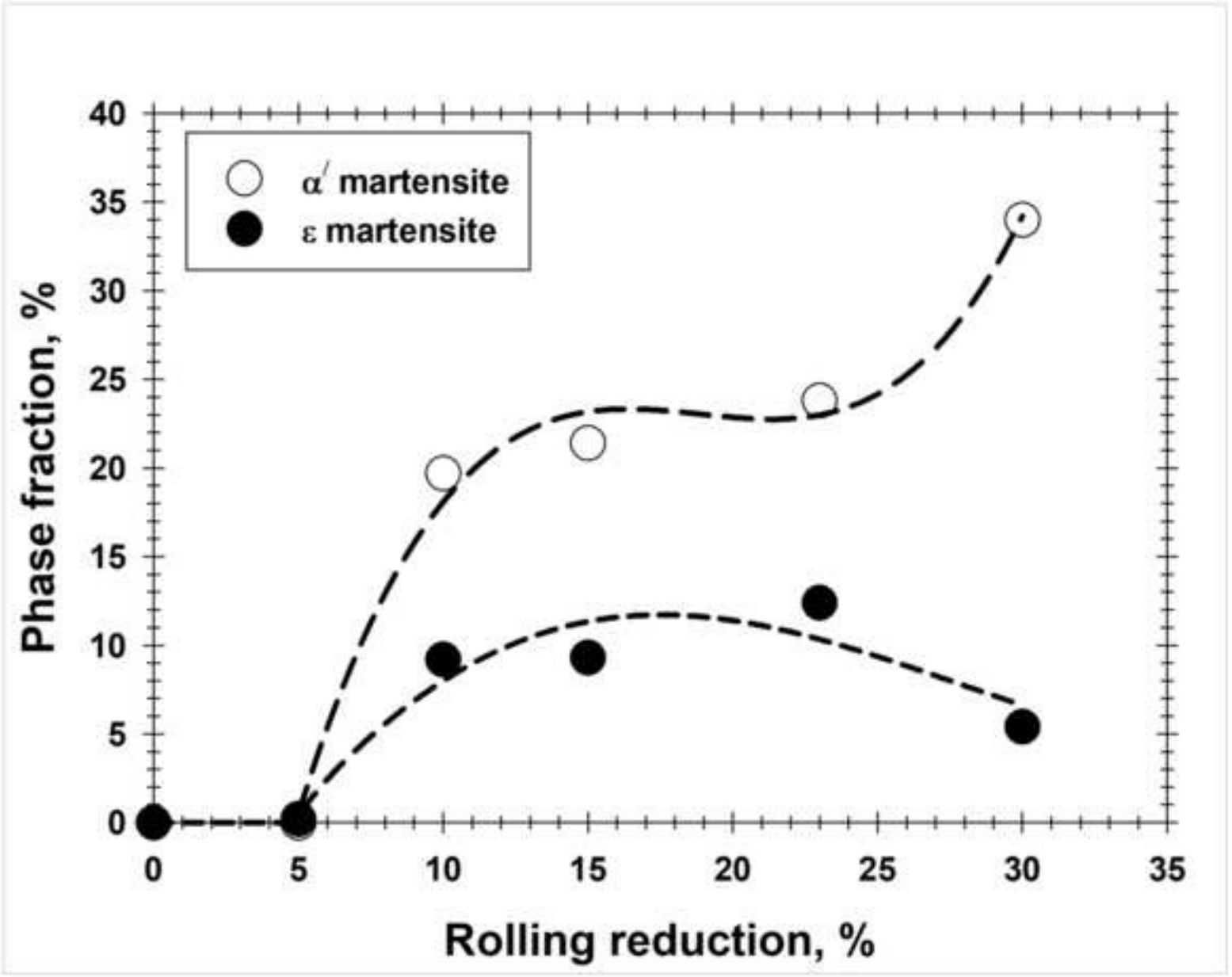


Figure 3. Effects of rolling reduction on the volume fraction of the martensitic phases

ACCEPTED MANUSCRIPT

Figure(s)

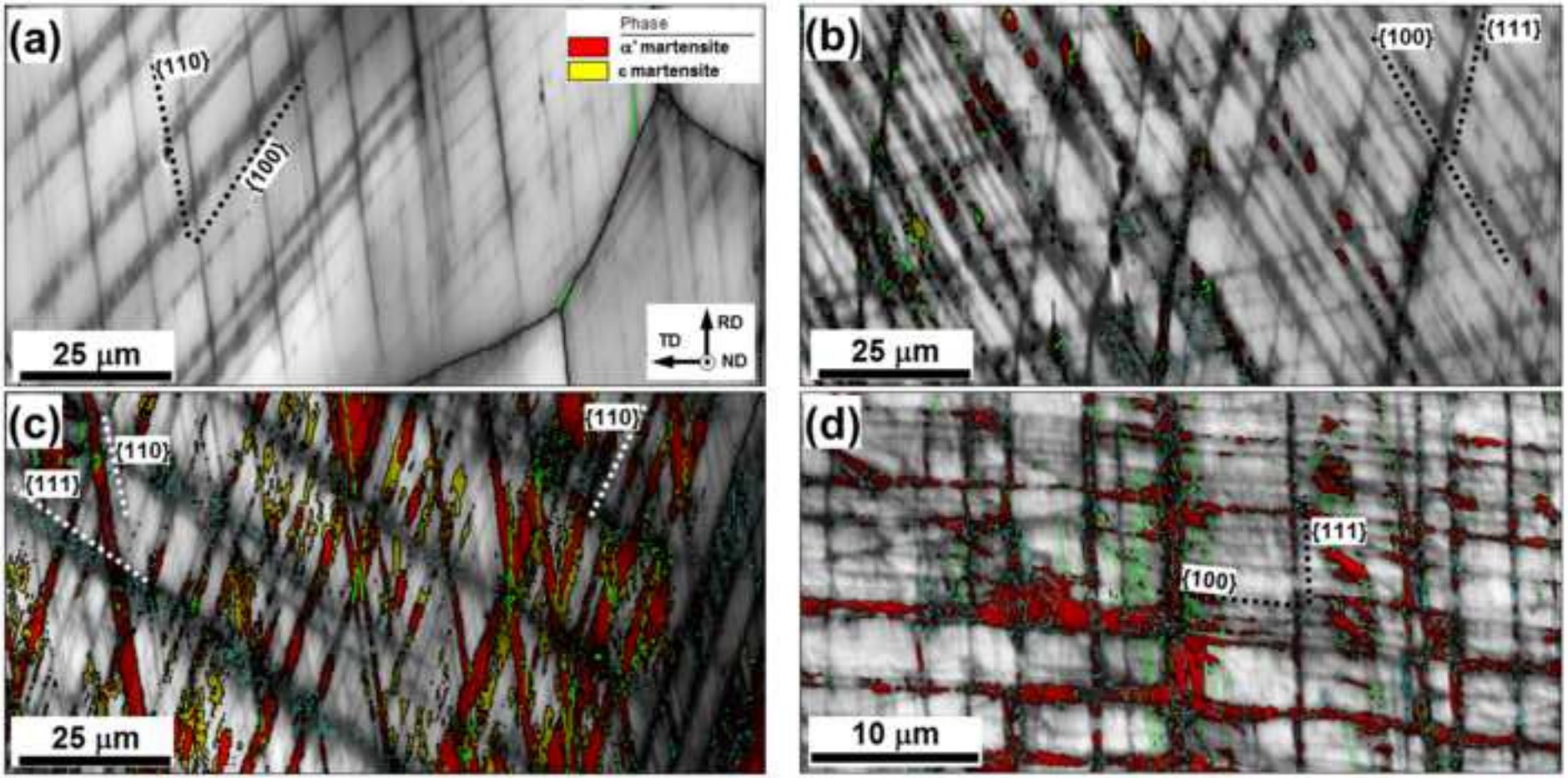


Figure 4. Selected portions of high-resolution EBSD Kikuchi-band-contrast maps showing the microstructures developed during a rolling reduction of (a) 5 pct., (b) 10 pct., (c) 15 pct., or (d) 30 pct. The color codes for the martensitic phases are given in the top right corner of (a). In the maps, low-angle boundaries are depicted as blue lines, high-angle (or phase) boundaries as black lines and Σ3 boundaries as green lines. The dotted lines indicate the traces of 111, 110 and 100 planes which are closest to the corresponding deformation-band trace.

ACCEPTED MANUSCRIPT

Figure(s)

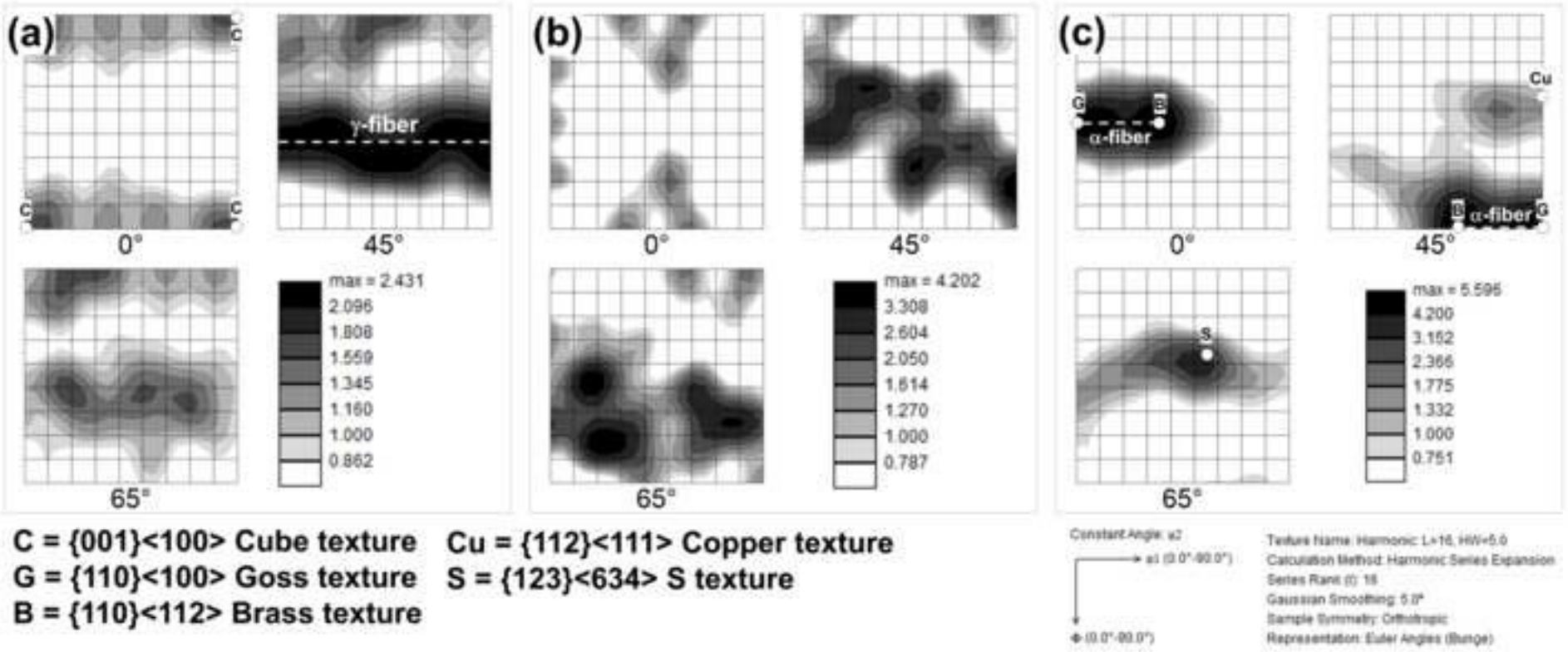


Figure 5. Selected sections (φ_2=0°, φ_2=45° and φ_2=65°) of orientation distribution functions (ODFs) showing the texture in the *austenite*: (a) base-metal condition, (b) after 10 pct. reduction (i.e. shortly after initiation of the martensitic transformation), or (c) after 30 pct. reduction. For comparative purposes, several ideal rolling orientations are superimposed the ODFs

ACCEPTED MANUSCRIPT

Figure(s)

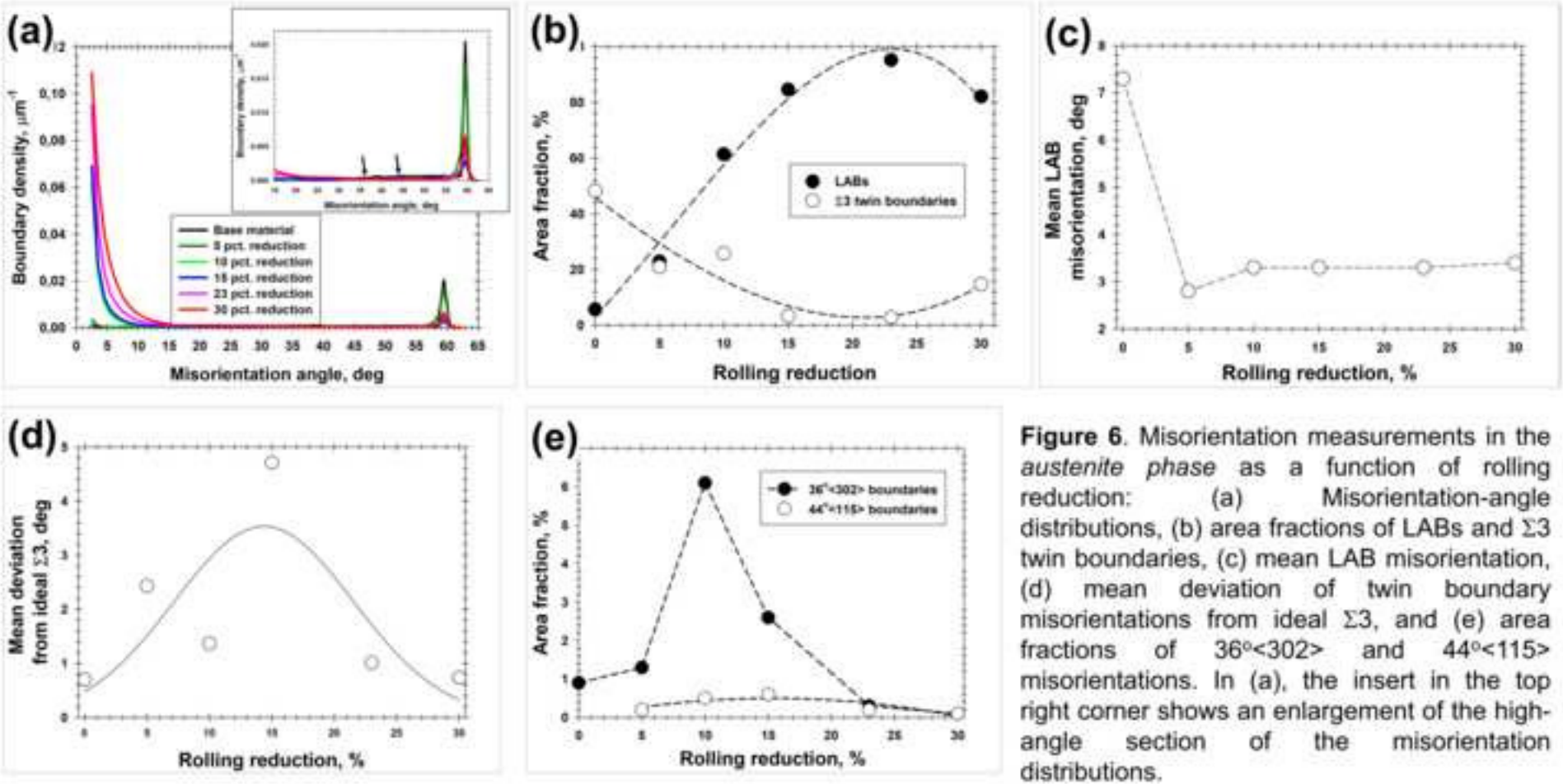


Figure 6. Misorientation measurements in the *austenite phase* as a function of rolling reduction: (a) Misorientation-angle distributions, (b) area fractions of LABs and Σ3 twin boundaries, (c) mean LAB misorientation, (d) mean deviation of twin boundary misorientations from ideal Σ3, and (e) area fractions of 36°<302> and 44°<115> misorientations. In (a), the insert in the top right corner shows an enlargement of the high-angle section of the misorientation distributions.

ACCEPTED MANUSCRIPT

Figure(s)

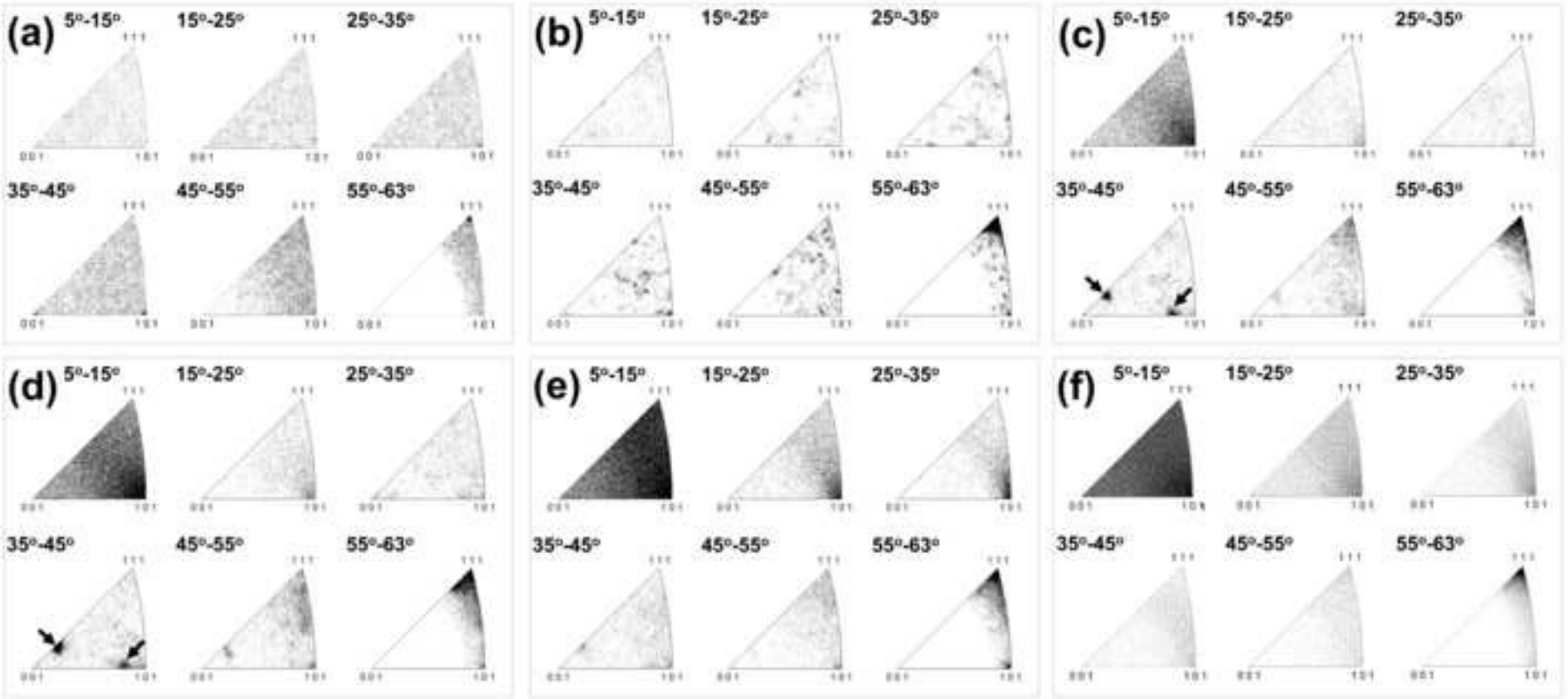


Figure 7. Effect of rolling reduction on misorientation-axis distribution in the *austenite* phase: (a) base material or after a rolling reduction of (b) 5 pct., (c) 10 pct., (d) 15 pct., (e) 23 pct., or (f) 30 pct.

ACCEPTED MANUSCRIPT

Figure(s)

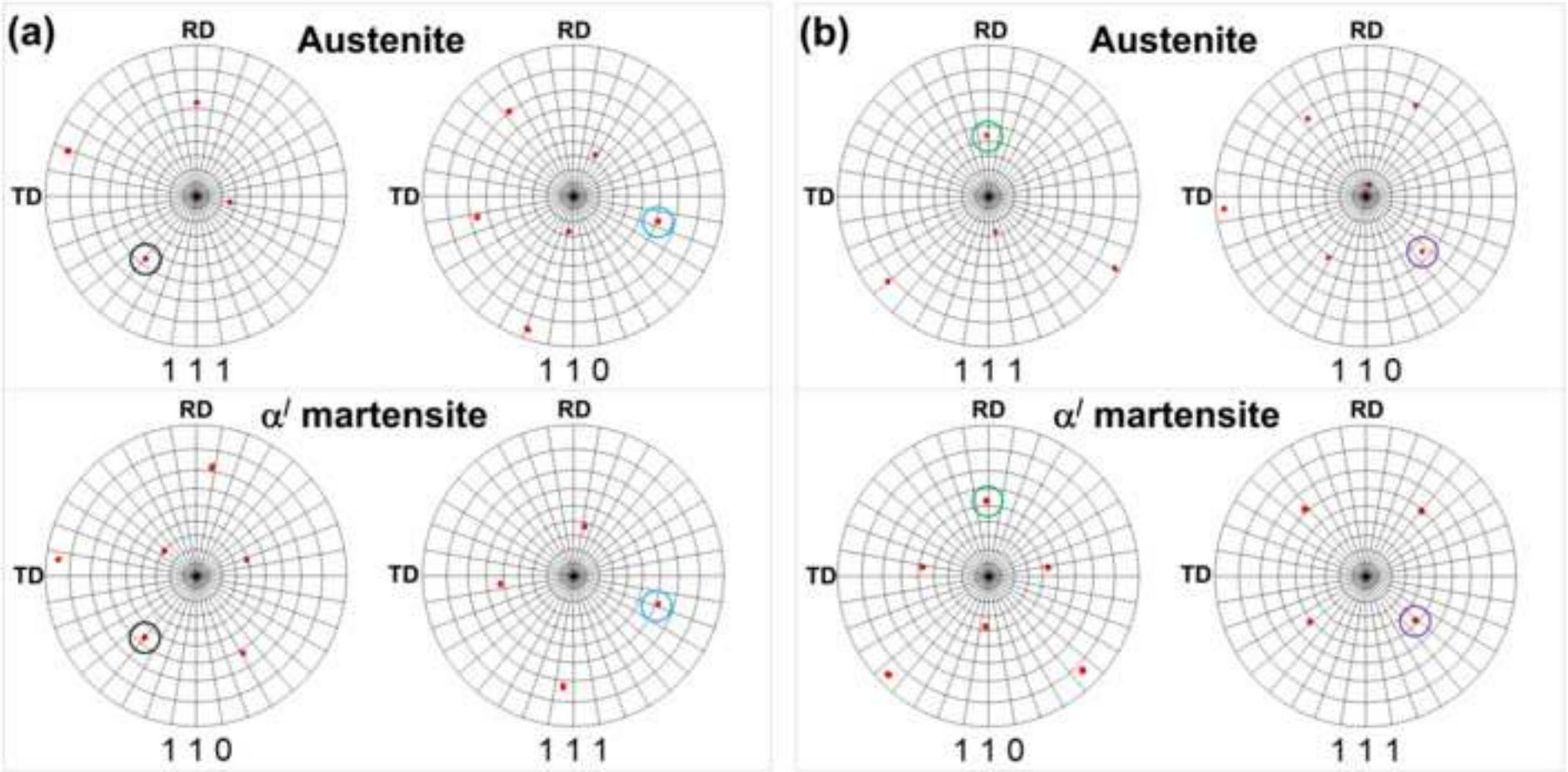


Figure 8. Typical examples showing the local orientation relationship between austenite and α' martensite as function of rolling reduction: (a) 10 pct. (i.e., shortly after initiation of martensitic transformation) or (b) 30 pct. In the pole figures, the closest related directions in the austenite and the α' martensite are circled.

ACCEPTED MANUSCRIPT

Figure(s)

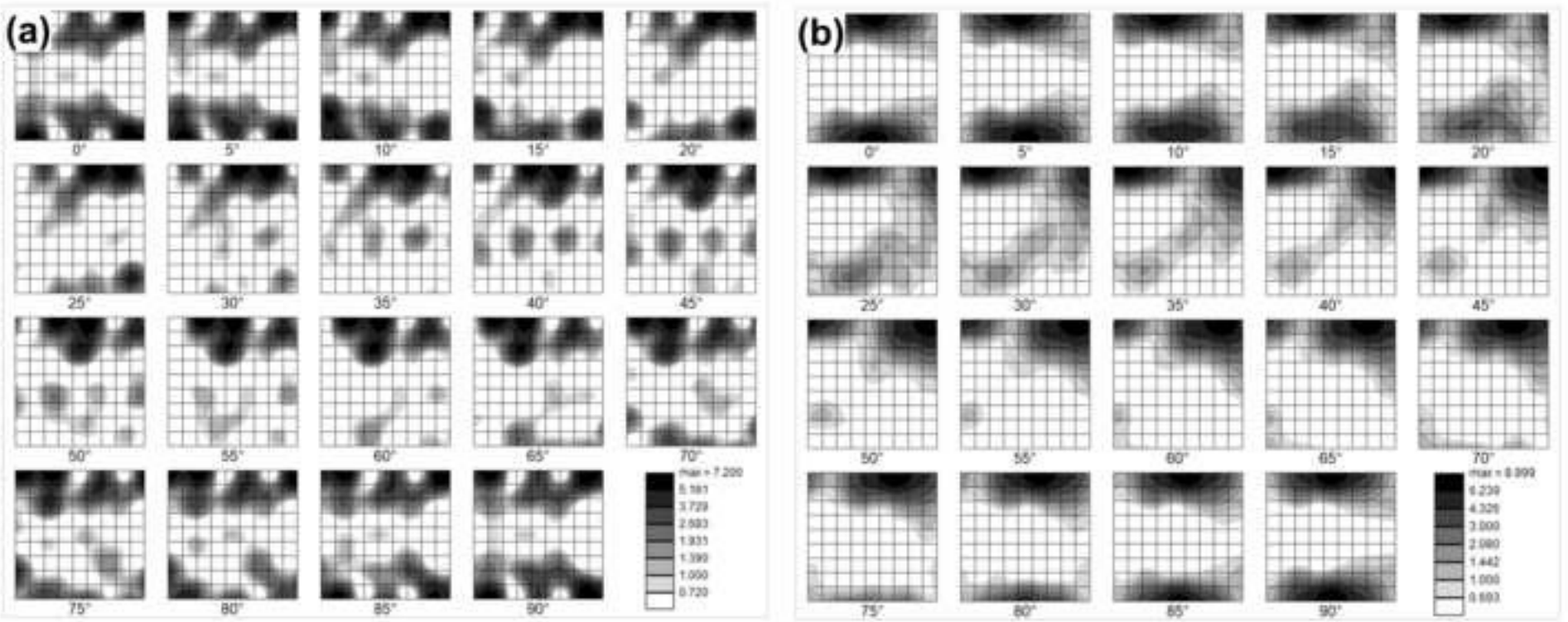
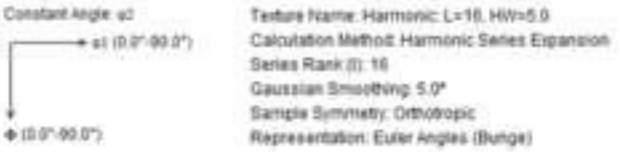


Figure 9. ODFs showing texture in α' *martensite* as function of rolling reduction: (a) 10 pct. rolling (i.e., shortly after initiation of martensitic transformation) or (b) 30 pct.



ACCEPTED MANUSCRIPT

Figure(s)

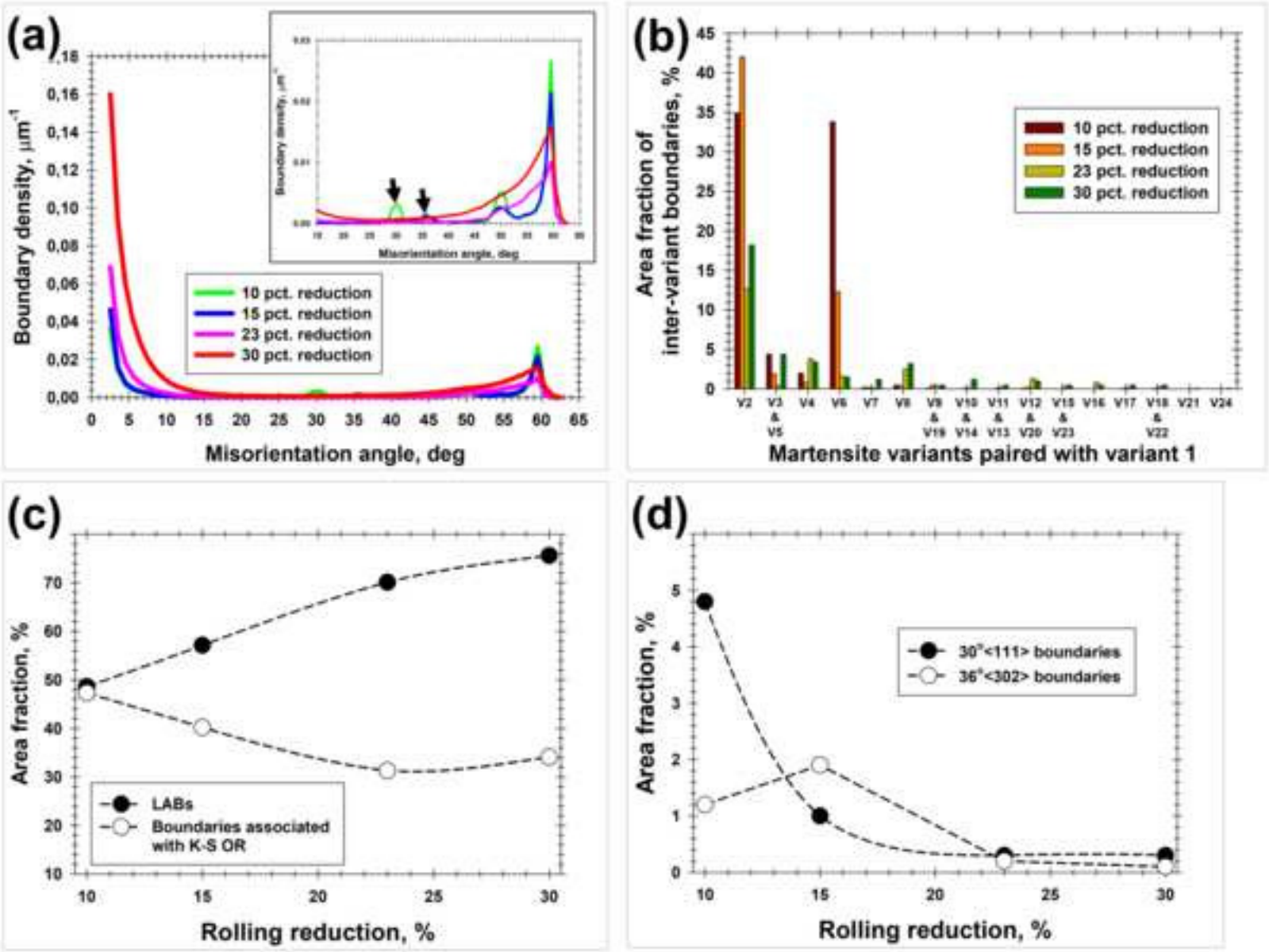


Figure 10. Misorientation measurements in *α′ martensite* as a function of rolling reduction: (a) misorientation-angle distributions, (b) variant-pairing frequency diagram according to the Kurdjumov-Sachs (K-S) orientation relationship, (c) area fractions of LABs and inter-variant boundaries, and (d) 30°<111> and 36°<302> misorientations. In (a), the insert in the top right corner shows an enlargement of the high-angle section of the misorientation distributions.

ACCEPTED MANUSCRIPT

Figure(s)

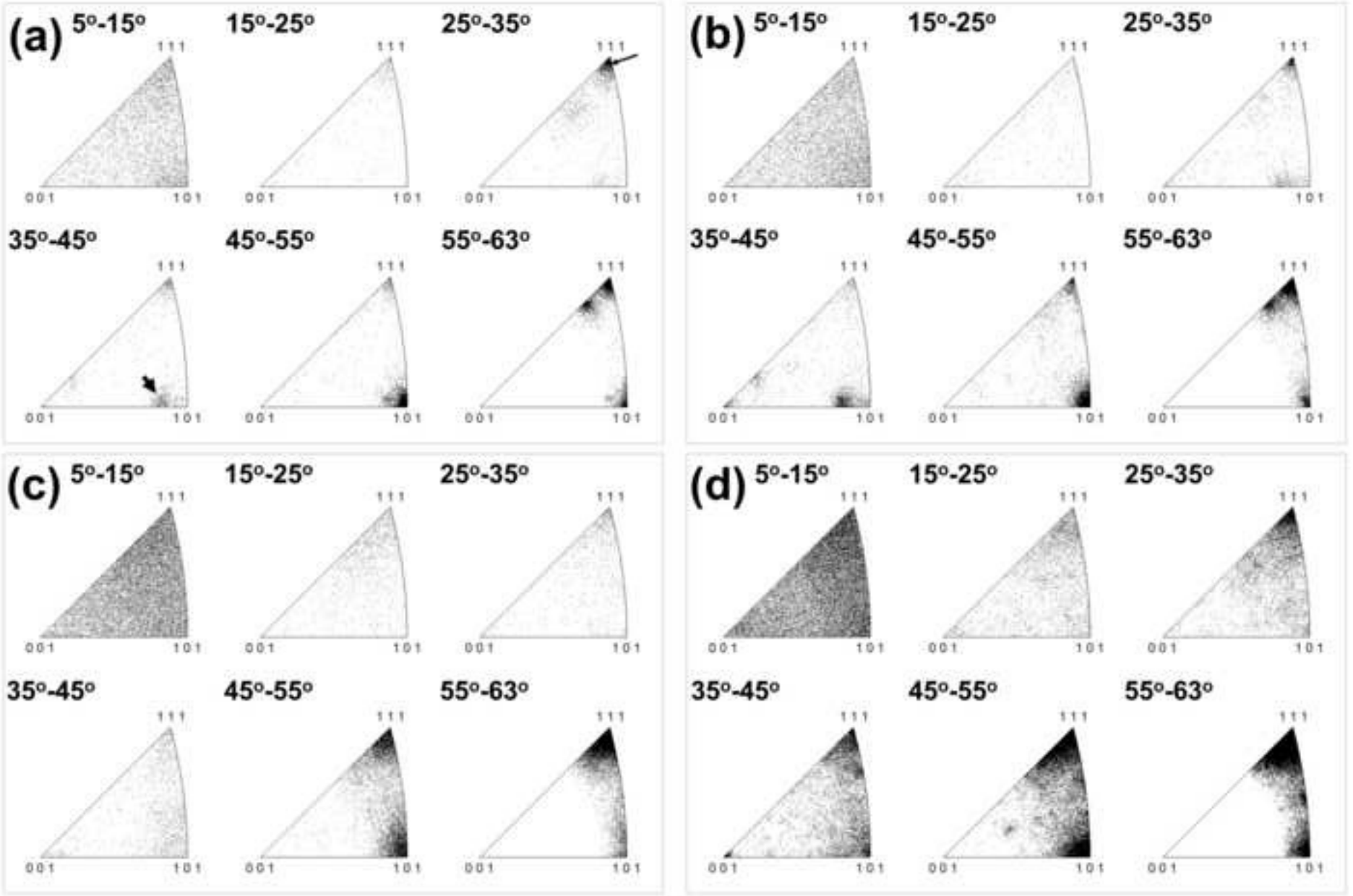


Figure 11. Effect of rolling reduction on misorientation-axis distribution in *α-martensite* after a reduction of: (a) 10 pct., (b) 15 pct., (c) 23 pct., or (d) 30 pct.

ACCEPTED MANUSCRIPT

Figure(s)

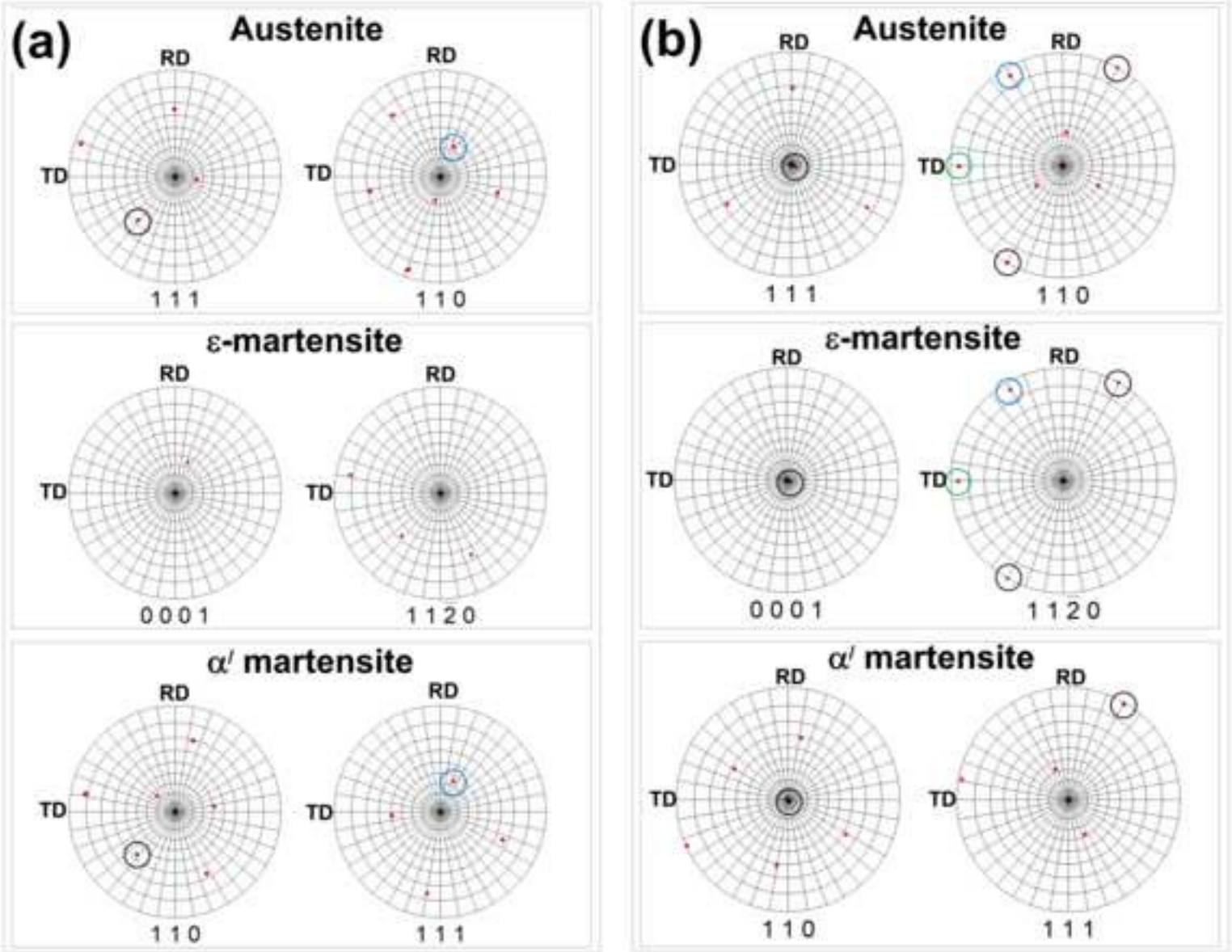


Figure 12. Typical examples showing the local orientation relationship between austenite, ε martensite and α' martensite: (a) the lack of a clear orientation relationship between the austenite and ε martensite, and (b) a nearly ideal Shoji-Nishiyama orientation relationship between the austenite and ε martensite. In the pole figures, the closest related directions in the austenite, ε martensite and α' martensite are circled. In (a), the data were taken after 10-pct. reduction (i.e., shortly after initiation of martensitic transformations), whereas the data in (b) were obtained from the material subjected to 30-pct. reduction.

ACCEPTED MANUSCRIPT

Figure(s)

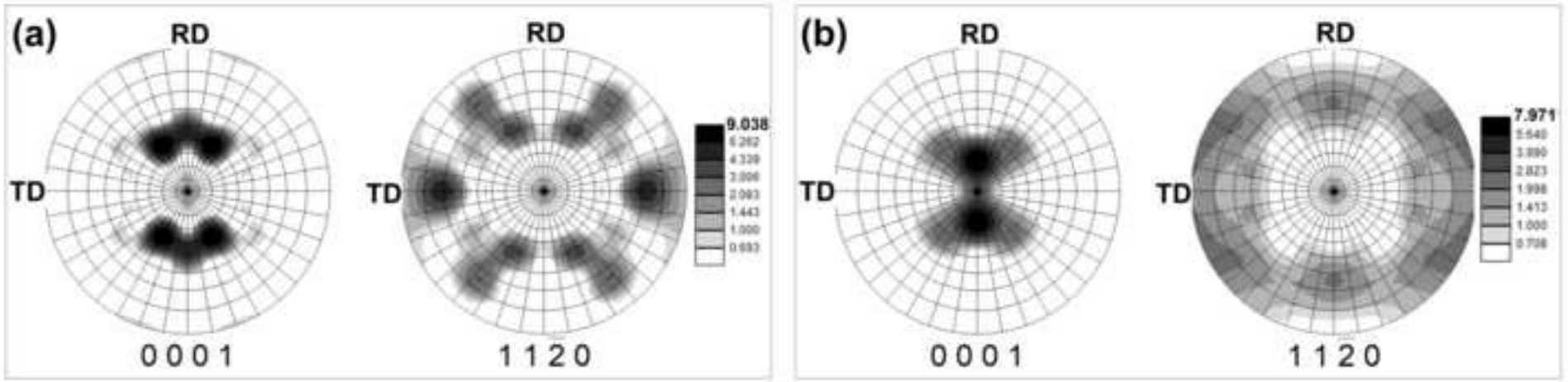


Figure 13. 0001 and 11-20 pole figures showing the texture in *ε-martensite* as function of rolling reduction: (a) 10 pct. (i.e., shortly after initiation of martensitic transformation) or (b) 30 pct.

ACCEPTED MANUSCRIPT

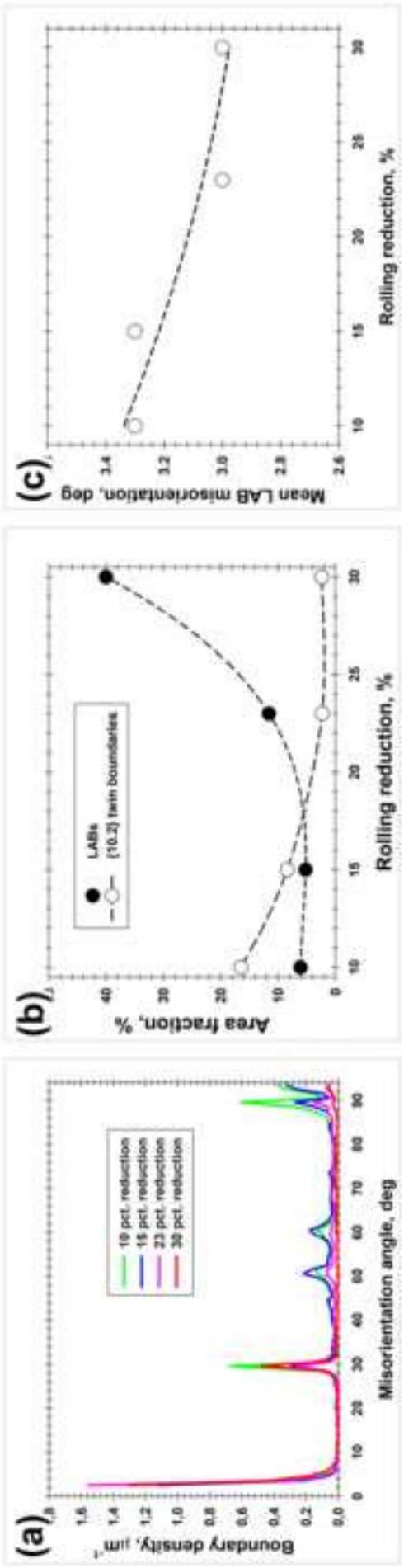


Figure 14. Misorientation measurements in *ε-martensite* as function of rolling reduction: (a) misorientation-angle distributions, (b) area fractions of LABs and {1012} twin boundaries, and (c) mean LAB misorientation.

Acc ript

Figure(s)

Figure(s)

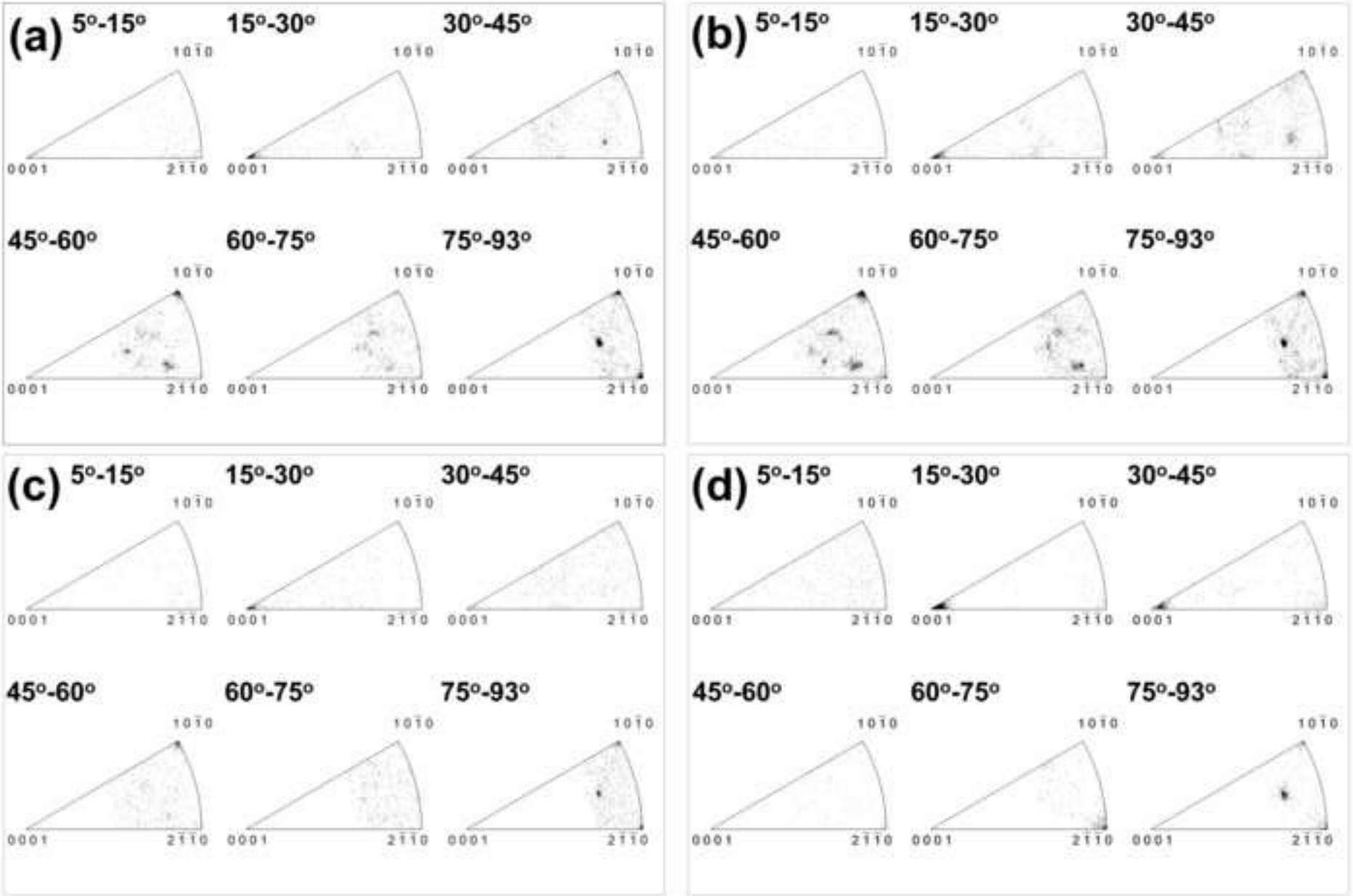
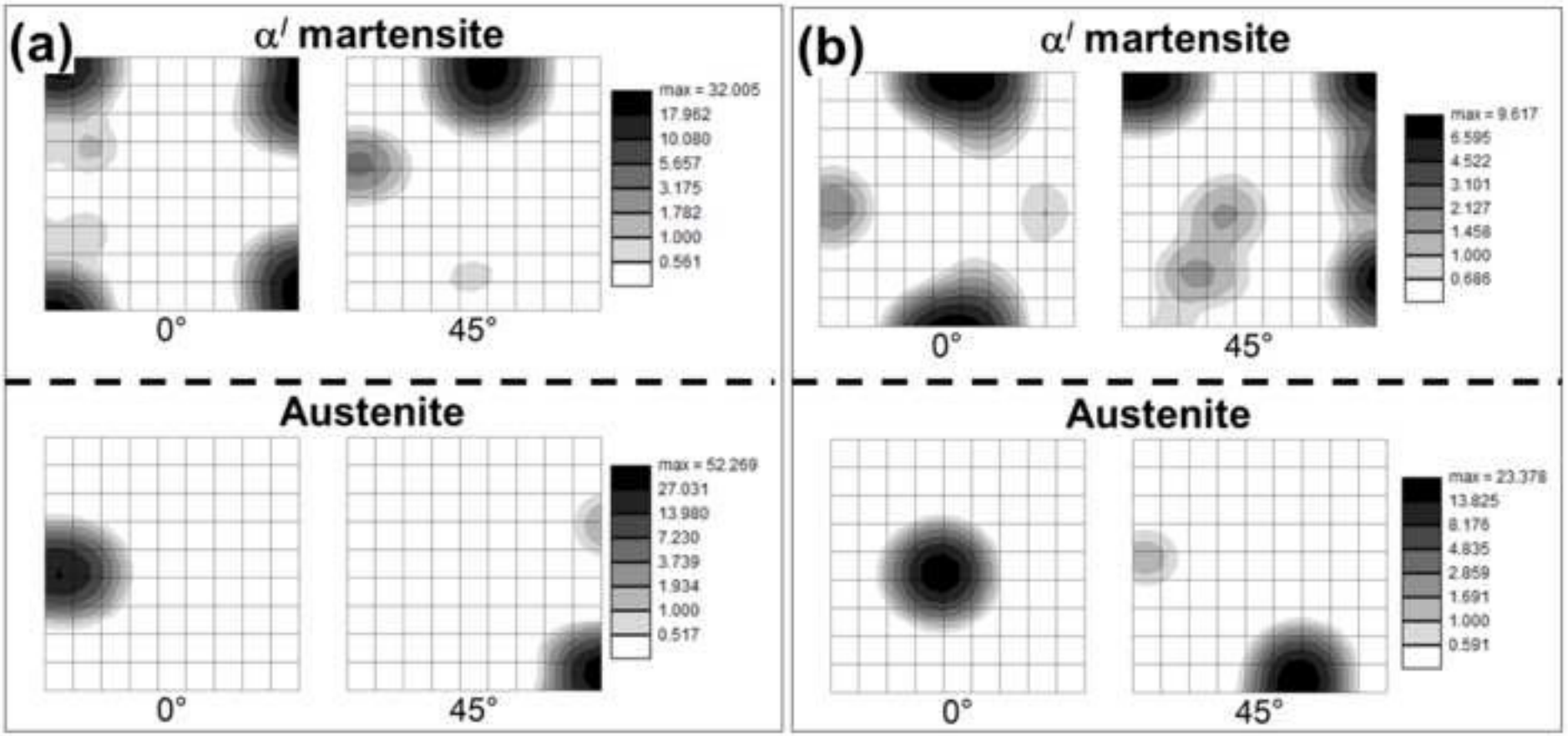


Figure 15. Effect of rolling reduction on misorientation-axis distribution in *ε-martensite* after a reduction of: (a) 10 pct., (b) 15 pct., (c) 23 pct., or (d) 30 pct.

ACCEPTED MANUSCRIPT

Figure(s)



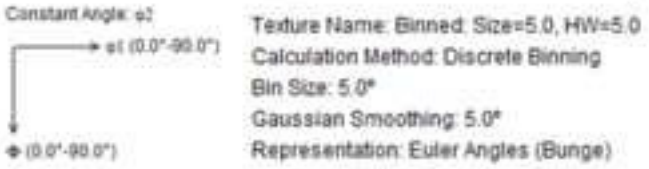


Figure 16. Selected sections (φ_2=0° and φ_2=45°) of ODFs illustrating the orientation relationship between α' martensite and austenite measured in the martensite domain with a crystallographic orientation close to (a) (0°;0°;0°) or (b) (0°;0°;45°). In both cases, the orientation data were taken from material rolled to a 30-pct.-reduction. Note: Subtle secondary texture components are also present in austenitic and martensitic phases in both cases.

ACCEPTED MANUSCRIPT